Non-Noble-Metal-Based Electrocatalysts Towards the Oxygen Evolution Reaction

*Zhi-Peng Wu, Xue Feng Lu, Shuang-Quan Zang, and Xiong Wen (David) Lou**

Dr. Z. P. Wu, Dr. X. F. Lu, Prof. X. W. Lou

School of Chemical and Biomedical Engineering, Nanyang Technological University, 62 Nanyang Drive, Singapore, 637459, Singapore

Email: xwlou@ntu.edu.sg; Webpage: http://www.ntu.edu.sg/home/xwlou/

Dr. Z. P. Wu, Prof. S. Q. Zang

Green Catalysis Center, and College of Chemistry, Zhengzhou University, Zhengzhou 450001, P.R. China.

Email: zangsqzg@zzu.edu.cn

Abstract

The development of low-cost, high-efficiency, and robust electrocatalysts for the oxygen evolution reaction (OER) is urgently needed to address the energy crisis. In recent years, non-noble-metal-based OER electrocatalysts have attracted tremendous research attention. Beginning with the introduction of some evaluation criteria for the OER, we review the current OER electrocatalysts with the classification of metals/alloys, oxides, hydroxides, chalcogenides, phosphides, phosphates/borates, and other compounds, along with their advantages and shortcomings. The current knowledge of the reaction mechanisms and practical applications of the OER are also summarized for developing more efficient OER electrocatalysts. Finally, the current states, challenges, and some perspectives for non-noble-metal-based OER electrocatalysts are discussed.

Keywords: Electrocatalysis; oxygen evolution reaction; non-noble-metal; mechanism; application.

1. Introduction

The global ever-increasing energy demand accompanied by the gradual depletion of fossil fuels and the deteriorating environment has stimulated an urgent hunt for renewable energy sources, such as wind and solar power.[1,2] However, those sustainable energy sources are usually intermittent with a time gap between the supply and demand.[3] As a result, energy conversion and storage technologies, such as water electrolysis which converts electric energies generated from solar and wind power into hydrogen fuels,[4,5] rechargeable metal-air batteries which possess exceptionally high energy density and exhibit low cost, environmental benignity and safety,[6,7] and reversible fuel cells which can also produce hydrogen fuel via electrochemical process,[8] are hence greatly required to achieve a sustainable energy landscape. Governed by the electrochemical reactions, the advancement of those energy conversion and storage systems is significantly impeded by the sluggish kinetics of the oxygen evolution reaction (OER), oxygen reduction reaction (ORR), and hydrogen evolution reaction (HER).[9-15] In particular, the OER, which can be applied to a wide range of energy conversion and storage technologies, serves as one of the most challenge conundrums and has attracted tremendous research attention in the past decades.

A complete OER process generates molecular oxygen together with several proton and electron couples transferred. The current OER electrocatalysts at the industrial level are highly dependent on the noble metal catalysts, primarily iridium (Ir) and ruthenium (Ru) based catalysts in acidic conditions. However, the large-scale commercialization of the noble-metal-based OER electrocatalysts is greatly hindered by their high cost, low crustal reserve, and relatively poor performance.[16,17] This serves as a strong driving force applied to stimulate the investigations of non-noble-metal-based OER electrocatalysts. In general, it is a great challenge for

non-noble-metal-based electrocatalysts to work stably in acidic media. Fortunately, some non-noble-metal-based OER electrocatalysts, for instance, manganese oxide,[18] earth-abundant metal phosphates and borates,[19-21] are recently reported to be capable of catalyzing OER in both neutral and acidic conditions. It is even more exciting to note that in alkaline conditions, some non-noble-metal-based electrocatalysts are able to catalyze OER with remarkable catalytic performance and often outperform the noble-metal-based electrocatalysts.[6,22] For this reason, we put primary focus on these non-noble-metal-based electrocatalysts in this review. To overcome the high overpotential of the OER, numerous non-noble-metal-based electrocatalysts have been developed, including metals/alloys,[23,24] oxides,[25-31] hydroxides,[32-37] chalcogenides,[38-42] phosphides,[5,43,44] phosphates/borates,[19,45,46] borides,[47] nitrites,[48,49] and other compounds.[50,51]

In this review, we start with the introduction of the evaluation criteria and methods for the OER (**Figure 1**). Then we summarize the recent advances of the non-noble-metal-based OER electrocatalysts in a classification of metals/alloys, oxides, hydroxides, chalcogenides, phosphides, phosphates/borates, and other compounds. Furthermore, to obtain an in-depth understanding of the OER reaction mechanism from the theoretical point of view, we provide some discussions of possible reaction pathways, the thermodynamic scaling relation and activity descriptors. The recent progress of the applications for the OER, such as, water electrolysis, rechargeable metal-air batteries, and reversible fuel cells, are also provided. Finally, this review is concluded with the current states and challenges, together with some possible solutions and future directions. We hope this review will provide some systematic insights for developing non-noble-metal-based OER electrocatalysts with high activity and stability, and will stimulate the research and development of OER-related technologies in the near future.

2. Evaluation criteria and methods for OER

The evaluation of the OER electrocatalytic performance requires benchmarking methodologies for a better comparison between different groups and institutes. Some key evaluating parameters which have been widely recognized are summarized as follows. The merits and demerits of these parameters for evaluation of the OER performance are also discussed.

2.1 Overpotential (η)

Overpotential (η), defined as the potential gap between the potential at a specific current density and the equilibrium potential (1.23 V), is one very important descriptor to evaluate the OER activity of the target electrocatalyst. To match a photoelectrochemical water splitting efficiency of 12.3%, a specific current density of 10 mA cm^{-2} is needed, where the overpotential here is defined as η_{10}. We note here that some OER electrocatalysts, *e.g.*, Ni- and Co-based materials, exhibit strong redox peaks at a potential range slightly above the equilibrium potential (1.23 V).[25,52] In principle, we should decouple the redox peak current from the OER current. Succinctly, the overpotential at a higher specific current density, *e.g.*, 100 mA cm^{-2} is selected for comparison. Overall, OER is a four-electron transfer process, a minimum theoretical potential of 1.23 V is required to overcome the thermodynamic barrier in each electron transfer step. However, as revealed by density functional theory (DFT) studies, some key intermediates (*O, *OH, and *OOH) involved in the OER process not always locate at the ideal position in the free energy diagram (refer to the reaction mechanisms section for details), which together with the kinetic reaction barriers contribute to the high overpotential of the OER.[53] The operation cell voltage (V_{op}) for water splitting can be described as Equation (1):

$$V_{op} = V_{eq} + \eta_a + |\eta_c| + IR \quad (1)$$

where V_{eq} denotes the potential under equilibrium condition (V_{eq} = 1.23 V), η_a and η_c represent the overpotentials required to overcome the kinetic barriers of the OER at the anode side and the HER at the cathode side, respectively. *IR* denotes the voltage drop for compensation of the internal resistance in the system. In other words, the overpotential of the overall water electrolysis is constituted by the overpotentials of OER (η_a) and HER (η_c), as well as the voltage drop caused by the system resistance (*i.e.*, *IR*), where the overpotential of the OER serves as the major barrier.[54]

2.2 Tafel slope

The Tafel equation correlates the overpotential and the current density in a logarithmic manner, which can be expressed as Equation (2)

$$\eta = a + b \times log\,(j) \quad (a = 2.303RTlogj_0/\alpha nF,\ b = 2.303RT/\alpha nF) \qquad (2)$$

where *b* denotes the Tafel slope, *j* represents the current density, j_o is the exchange current density (see 2.3 for details), *R* is the idea gas constant, *T* represents the absolute temperature, *n* is the number of transferred electrons during the redox reaction, *F* is the Faraday constant, and α is the charge transfer coefficient. In Equation (1), a small Tafel slope (*b*) indicates that a small overpotential change is required to meet a fast increase of the current density, and hence demonstrating excellent electrocatalytic kinetics. Currently, Tafel plots can be extracted by three methods, *i.e.*, voltammetry, chronoamperometry/chronopotentiometry and electrochemical impedance spectroscopy (EIS). First of all, voltammetry is the most widely used approach. However, it is unable to provide polarization curve at a steady state. In fact, they continually change with time. A low scan rate (no more than 5 mV s^{-1}) should be used in the voltammetry measurement to minimize the experimental inaccuracies as much as possible. When pronounced redox peaks appear in the voltammograms, the backward sweep of the voltammetry scan is suggested to be used for constructing the Tafel plot.[55] To obtain real steady-state

polarization curves, static electrochemical techniques, *e.g.*, amperometry/potentiometry in which sufficient time is given to achieve a steady state at the catalytic interface, can be applied. Tafel slopes measured by static electrochemical techniques do not reflect the intrinsic activity of the catalyst since the resistances of the catalyst and solution, as well as the resistance between the catalyst-substrate electrode interface still remain.[55] To address this issue, the EIS technique was developed by Hu and co-workers to avoid the influence of those resistances.[56] In the results, the logarithmic reciprocal of the charge transfer resistance is plotted against the overpotential. The Tafel slope yielded here excludes the influence of a series of resistances and reflects the intrinsic activity of the catalyst.[55] These three methods should be carefully selected and used on a case-by-case basis.

2.3 Exchange current density (j_0)

As mentioned in 2.2, the exchange current density (j_0) is another important descriptor of the OER kinetics, which reflects the intrinsic electron transfer rate between the electrode and the electrolyte. j_0 is the current density when η equals to zero without net electrolysis. Currently, j_0 cannot be directly measured by electrochemical methods and can only be calculated through the Tafel equation as illustrated in Equation (1). Usually, a good electrocatalyst exhibits a high j_0.

2.4 Turnover frequency (TOF)

The turnover frequency (TOF) describes the intrinsic catalytic activity of the catalyst, which is defined as the rate at which the number of the generated products normalized on the number of active sites. TOF can be calculated by Equation (3) for an electrocatalytic reaction involving gas evolution.

$$\mathrm{TOF} = jN_A/nF\Gamma \quad (3)$$

Where N_A is the Avogadro constant, Γ is the surface or the total concentration of active sites or the

number of participated atoms. However, in practice, it is hard to examine the precise number of active sites, especially on solid-state heterogeneous electrocatalysts. The number of active sites is often overestimated by counting the total active species involved in the electrochemical system including those of the chemically inert or buried species. Some researchers also reported the TOF values based on the readily accessible active sites or the surface sites assessed by indirect measurement approaches.[55,57] An appropriate method for calculating the TOF values of OER based on 3d transition metal electrocatalysts is to integrate the redox peak area for the reaction of oxide/hydroxide to oxyhydroxide.[58] In this instance, only the metal sites directly participated in the *in situ* redox reaction are assumed to be the active sites.[55]

2.5 Faraday efficiency (FE)

The Faraday efficiency (FE) refers to the electron conversion efficiency to generate products, such as molecular O_2 and H_2. The FE of the OER is the ratio between experimental and theoretical values of oxygen production. Generally, there are two methods for determining the FE of the OER. In the first method, the theoretically yielded quantity of O_2 is calculated via the integration of the chronoamperometric or chronopotentiometric analysis. The quantity of the practically generated O_2 gas is measured through the conventional water-gas displacement method, the gas chromatography, or the fluorescence spectroscopy.[59] The other method is based on the rotating ring disc electrode (RRDE), in which a finely-polished glassy carbon disk and Pt ring assembly is used. The same potential window for the OER is applied to the disk region, while a constant potential for the ORR is set on the Pt ring.[59] The following Equation (4) can be used to calculate the FE:

$$\mathrm{FE} = I_R\, n_D / I_D n_R\, N_{CL} \quad (4)$$

Where I_R and I_D represent the currents obtained from the ring and disc, respectively. n_R and n_D denote

the numbers of electrons transferred at the ring and disc regions, respectively, which are both 4 in the case of OER by definition. N_{CL} is the collection efficiency of the RRDE.

2.6 Electrochemically active surface area (ECSA)

The electrochemically active surface area (ECSA) is highly dependent on varying electrochemical processes and catalytic materials. There are a few methods to measure the ECSA for different materials, such as integrating the redox peak area (mainly for 3d transition metal-based catalysts), hydrogen underpotential deposition, carbon monoxide stripping, and the double layer capacitance. The evaluation method and result of the ECSA are often different on varying electrochemical reactions and materials. The ECSA of a material should not serve as a crucial criterion for comparing the activity in different studies. Instead, it is suggested to use the ESCA for comparisons of similar materials in the same study.

2.7 Mass and specific activities

The mass activity (MA) is defined as the current normalized on the mass loading of the target catalyst at a specific overpotential, which is gaining importance in evaluating the catalytic performance of OER electrocatalysts, especially when considering the catalyst costs. Thus, the MA is more often used as a key evaluation parameter for noble-metal-based materials but less important for non-noble-metal-based catalysts. The other crucial evaluation parameter for OER is the specific activity (SA), which is usually normalized on the geometrical area of the electrode, Brunauer–Emmett–Teller (BET) surface area or ECSA of the catalyst. The geometrical area normalized SA is only suitable for planar and smooth surfaces, while the BET surface area normalized SA often results in inappropriate estimations since the BET measured surface area is based on N_2 adsorption and

desorption, which is not necessarily electrochemically active. The SA value normalized on ECSA is more meaningful in reflecting the real activity of the catalyst, which has thus gained more attention over the former ones.[55,60] Unfortunately, the accurate measurement and comparison of ECSA for different materials are somehow difficult, which makes the ECSA normalized SA a less practical evaluation parameter. In addition, a benchmarking overpotential should be defined to determine the MA and SA for a better comparison.

2.8 Stability

High stability is required to meet the demand for practical applications. In some cases, high stability is established on the sacrifice of the activity. The non-noble-metal-based OER electrocatalysts often exhibit excellent stability in alkaline conditions but suffer from the poor durability in acidic media. There are some typical methods for evaluating the stability of an electrocatalyst. The accelerated durability test by conducting cyclic voltammetry (CV) cycling (usually hundreds to thousands of cycles) at a high scan rate is commonly used. Before and after the rapid CV cycling, the linear sweep voltammetry (LSV) is carried out to examine the overpotential shift at a specific current density (*e.g.*, 10 mA cm^{-2}). The smaller overpotential shift represents the better stability. Two other widely used methods are chronoamperometry (I-t curve at a constant potential) and chronopotentiometry (E-t curve at a fixed current density). A stable current density at a fixed potential by chronoamperometry or a negligible overpotential increase at a fixed current density by chronopotentiometry is recognized to be stable for the scaling up of water electrolysers.[55,59] The stability issue under high current densities (50 or 100 mA cm^{-2}) needs to be addressed urgently to realize the large-scale commercialization of noble-metal-free OER electrocatalysts.[61,62] In addition, the composition, morphology, and structure of the electrocatalysts should also be checked for evaluating the stability.[36,40,43]

3. Classification of the non-noble-metal-based OER electrocatalysts

Noble-metal-free OER electrocatalysts have attracted tremendous research attention and made a huge scientific stride in the past decades. In this section, we will highlight the recent advances of non-noble-metal-based (mainly Mn, Fe, Co, and Ni) OER electrocatalysts with a classification of metals/alloys, oxides, hydroxides, chalcogenides, phosphides, phosphates/borates, and other earth-abundant metal compounds. The synthetic strategy, electrocatalytic performance, structural characterization, and catalytic mechanism investigations are discussed in detail.

3.1 Metals/alloys

Non-noble-metal-based electrocatalysts in pure metallic state often cannot survive directly in harsh electrolytes including both acidic and alkaline media due to the strong corrosion effect. Therefore, they are usually, whether in monometallic or alloy states, embedded or decorated in the relatively stable hosts (such as carbon materials). Xu *et al*. fabricated a highly efficient OER electrocatalyst with Ni nanoparticles (NPs) encapsulated in N-doped graphene via readily annealing the metal-organic framework (MOF) material.[23] Metal alloys usually exhibit enhanced catalytic activities for reactions by harnessing the synergistic effect between metals.[63,64] Wang *et al*. prepared NiFe alloy NPs with different crystal phase structures coated with N-doped carbon shell.[63] The NiFe alloy catalyst with the hexagonal close-packed (hcp) phase exhibits an ultralow overpotential of 226 mV to drive a current density of 10 mA cm^{-2} for the OER. Besides the studies of small earth-abundant metal NPs, to maximize the atomic efficiency and improve the catalytic activity of the electrocatalysts, scientists have been focusing on exploring rooms in nanoclusters and single-atom catalysts.[65,66] Recently, Zhang *et al*. highlighted an efficient OER electrocatalyst with atomically distributed Ni sites on the

N-doped hollow carbon matrix (HCM@Ni-N).[17] As illustrated in **Figure 2**A, the synthetic process evolves a hard-template method followed by pyrolysis and acid etching processes to yield the final product. The morphology and structure of the HCM@Ni-N were characterized by transmission electron microscope (TEM) (Figure 2B), annular dark-field scanning transmission electron microscope (ADF-STEM) (Figure 2C), and high-angle annular dark-field scanning transmission electron microscope (HAADF-STEM) (Figure 2D) techniques, showing the uniformly distributed spherical hollow structures with atomically dispersed isolated Ni atoms throughout the particles. The HCM@Ni-N shows a much better OER performance comparing with other control catalysts (Figure 2E). As evidenced by the X-ray absorption spectroscopy (XAS) and DFT calculations, the boosted OER catalytic activity is originated from the effective electronic coupling between Ni and N, which can intrinsically decrease the Fermi level and adjust the adsorptions of key intermediates.

3.2 Oxides

Non-noble-metal-based oxides have attracted great attention in electrocatalysis applications, because of their affordable prices, abundant reverses, tunable structures, and stable properties. The strategies of controlling the morphology, manipulating the composition, tuning the electronic structure via foreign metal doping, and integrating hybrid structures into composites are found to be effective in fabricating highly efficient oxide-based OER electrocatalysts. In this section, we will briefly introduce some recently reported non-noble-metal-based oxide OER electrocatalysts, including single metal oxides (mainly Co, Ni, Cu, and Mn oxides), spinel oxides, and perovskite oxides.

The OER activities of the single non-noble-metal oxide electrocatalysts depend on the metal types, metal oxidation states, morphologies, and supports. In addition, the poor conductivity greatly hinders their applications to the OER. Two strategies are developed to address the poor conductivity

issue, including i) manipulating the structures and compositions of the oxides through doping heteroatoms, introducing oxygen vacancies, and forming polymetallic oxides; ii) incorporating conductive substrates (carbon material or metal substrate). For example, Tong *et al*. studied a strongly interacted Co oxide NPs and B,N-decorated graphene (CoO_x NPs/BNG) hybrid electrocatalyst prepared by thermal annealing the precursor under NH_3 atmosphere (**Figure 3**A).[67] Abundant and strong Co-N-C bridging bonds together with numerous oxygen vacancies act as the active sites, exhibit strong synergetic effect, and enhance the electron transfer efficiency. As such, the CoO_x NPs/BNG electrocatalyst shows a low overpotential of 295 mA at 10 mA cm^{-2} for the OER (Figure 3B). Liao *et al*. fabricated a nickel oxide (NiO) and carbon nitride hybrid nanocomposite through bridging the poorly conductive metal oxide and the semi-conductive carbonaceous material via forming Ni-N bonds.[26] The facilitated charge transport in catalysis boosts the electrocatalytic performance for the OER as shown in Figure 3C (overpotential of 261 mV at 10 mA cm^{-2}). Besides Ni and Co oxides, Cu oxides also show outstanding catalytic performance towards the OER. For example, Huan *et al*. prepared dendritic Cu/CuO hybrid nanostructures via electrodepositing CuO NPs on the conductive Cu foam substrate coated with a Cu oxide passivation layer (Figure 3D-F).[27] As shown in Figure 3G, the scanning transmission electron microscopy-X-ray energy-dispersive spectroscopy (STEM-XEDS) maps display a metallic Cu core and two consecutive Cu oxide passivation layer shells. The electrocatalyst exhibits a very low overpotential of 290 mV at 10 mA cm^{-2} as well as remarkable stability for the OER.

The family of spinel oxides has attracted substantial research attention as OER catalysts owing to their remarkable catalytic performance, high charge transfer efficiency, and high stability in harsh alkaline media and under high anodic electric potential.[68] The general formula of spinel oxides can

be described as AB_2O_4, where the cation A^{2+} occupies the center of a tetrahedral unit and the B^{3+} locates at the octahedral site. As bimetallic oxides for the OER, the most studied spinel oxides including MCo_2O_4 and MFe_2O_4 (M represents other non-noble metals) often exhibit better electrochemical performance for OER than that of the single metal oxide catalysts. Introducing oxygen vacancies into the OER electrocatalysts is an effective way to enhance their catalytic performance. As shown in **Figure 4**A, Peng *et al*. fabricated a chemically reduced $NiCo_2O_4$ (R-NCO) spinel oxide electrocatalyst with the multishelled hollow structure.[69] The reduced $NiCo_2O_4$ spinel oxide catalyst exhibits an ultralow overpotential of 240 mV at 10 mA cm^{-2} and a low Tafel slope of 50 mV dec^{-1}, which is superior to both of the as-prepared $NiCo_2O_4$ spinel oxide and the state-of-the-art RuO_2 catalysts (Figure 4B). DFT calculations reveal that the binding energies of some key intermediates during the oxygen evolution process are optimized by the participation of oxygen vacancies (Figure 4C). An efficient hybrid electrocatalyst consisting of carbon-supported $CoFe_2O_4$ spinel nanorod arrays and N-doped carbon coated Ni foam substrate was fabricated by Lu *et al*. via a facile one-step pyrolysis approach on MOFs.[22] A representative TEM image (Figure 4D) shows that the porous nanorod is consisted of small NPs, which is believed to be beneficial for the improved surface area and the enhanced gas bubble fluidity. The hybrid nanomaterial consisting abundant oxygen vacancies exhibits excellent electrocatalytic performance for OER with a low overpotential of 240 mV at 10 mA cm^{-2} (Figure 4E) and an increase of only 7.5% in potential at 100 mA cm^{-2} after the 60 h durability test. Sun *et al*. synthesized N, P, and F tri-doped $CoFe_2O_4$ spinel oxide anchored with MoS_2 nanoclusters.[70] The incorporations of the heteroatom dopants and MoS_2 NPs modulate the electronic structure of the electrocatalyst, produce abundant oxygen vacancies and active sites, and increase the active surface area. The hybrid nanomaterial enriched with oxygen vacancies exhibits an

overpotential of 250 mV at 10 mA cm^{-2}.Other spinel oxide OER electrocatalysts mainly include MMn_2O_4, MCr_2O_4, inverse spinel oxides, ternary metallic spinel oxides, and spinel oxide constructed with other metal oxide to form hybrid structures, which also exhibit extraordinary OER performance.[29,71] For example, Wang *et al*. recently designed a hybrid-MOF-assisted method to synthesize novel Co_3O_4/Co-Fe oxide double-shelled nanoboxes (Co_3O_4/Co-Fe oxide DSNBs).[72] The starting precursor, zeolitic imidazolate framework-67 (ZIF-67), is converted into ZIF-67/Co-Fe Prussian blue analog (PBA) yolk-shell nanocubes via a facile ion-exchange reaction with the assistance of $[Fe(CN)_6]^{3-}$ ions. Then a following thermochemical treatment on the hybrid precursors yields the Co_3O_4/Co-Fe oxide DSNBs. As shown by the TEM image in Figure 4F, hierarchically double-shelled structures can be observed clearly. The elemental analysis by HAADF-STEM is shown in Figure 4G. Fe, Co, and O elements are all uniformly distributed throughout the outer shell, while only evenly distributed Co and O elements are shown in the inner shell. The Co_3O_4/Co-Fe oxide DSNBs shows a low overpotential of 297 mV to obtain a current density of 10 mA cm^{-2}, outperforming other catalysts (Figure 4H). The excellent OER performance is thought to be originated from the structural and compositional merits of the material.

Perovskite oxides with a general formula of ABO_3, where A is commonly rare-earth or alkaline-earth metal and B represents transition metals, have been widely investigated as promising non-noble-metal-based electrocatalysts for energy conversion and storage applications.[73,74] In principle, perovskite oxides can be described as $A^{2+}B^{4+}O_3$, $A^{3+}B^{3+}O_3$, or other types. Owing to their highly tunable metal combinations and compositions, unique 3d electronic structures, and high stability, perovskite oxides exhibit remarkable catalytic activities for the OER. Li *et al*. studied the roles of covalent bonding and separation of surface oxygen on OER on $CaCoO_3$ and $SrCoO_3$ cubic

perovskite oxides catalysts.[30] Both perovskite catalysts share similar Co^{4+} intermediate spin state which is responsible for the similar onset potential for the OER. However, $CaCoO_3$ shows better electrochemical activity and stability for the OER due to its smaller lattice constant and shorter surface oxygen separation, comparing with that of $SrCoO_3$. The formation of surface peroxide $(O_2)^{2-}$ intermediate was considered as the rate-determining step (RDS) for the OER. Double perovskite oxide catalysts, usually in a formula of AA'BB'O_6, exhibit excellent catalytic performance for OER due to their diverse electronic structures and strong synergistic effects. Double perovskite $LaFe_xNi_{1-x}O_3$ (LFNO) nanorods were synthesized by Wang *et al*. via a sol-gel approach.[75] The increased surface area, optimized electronic structure, and the strong coupling between Ni and lattice oxygen contribute simultaneously to the enhanced electrochemical performance of the catalyst for OER. By regulating the Ni/Fe ratio in the perovskite oxide catalysts, a low overpotential of 302 mV at 10 mA cm^{-2} (Figure 4I) and a 20 h stability performance with negligible current decay were achieved.

3.3 Hydroxides

Non-noble-metal-based hydroxide electrocatalysts, mainly containing first-row transition metals (Fe, Co, and Ni *etc.*), are a group of pivotal efficient electrocatalysts for the OER and have attracted enormous interest in recent years. In this section, we briefly classify and introduce the non-noble-metal hydroxide electrocatalysts in terms of three representative groups, *i.e.*, hydroxides, layered double hydroxides (LDHs), and oxyhydroxides.

The representative non-noble-metal hydroxides as OER electrocatalysts are $Ni(OH)_2$, $Co(OH)_2$, and $Ni_xFe_{1-x}(OH)_2$. For instance, McAteer *et al*. synthesized liquid exfoliated $Co(OH)_2$ nanosheets with different sizes.[76] The smallest $Co(OH)_2$ nanosheet outperforms other nanosheets with bigger sizes, indicating the nanosheet edges as the active sites for the OER. Similarly, as highlighted by Zhou

et al., $Ni_{0.83}Fe_{0.17}(OH)_2$ prepared by introducing Fe into $Ni(OH)_2$ nanosheets via a cation-exchange method shows a thin nanosheet morphology (**Figure 5**A) with abundant nanopores (Figure 5B), which is believed to be responsible for the enriched active sites.[77] The uniform elemental distribution substantiates that this cation-exchange approach is effective to achieve uniform Fe doping in $Ni(OH)_2$ nanosheets (Figure 5C). $Ni_{0.83}Fe_{0.17}(OH)_2$ shows the best catalytic OER activity comparing with $Ni(OH)_2$, NiFe LDH, and $Ni_xFe_{1-x}(OH)_2$ with other metal ratios (Figure 5D). The excellent OER activity can be attributed to the enriched active surface sites, abundant defects, and enhanced surface wettability. This strategy offers a new path for fabrication of highly effective OER catalysts.

Co/Ni-based LDH catalysts represent a group of promising electrocatalysts towards the OER owing to their highly tunable structures and compositions, unique physicochemical properties, and remarkable catalytic performance. Increasing the number of the active sites is the most straightforward and effective strategy to enhance the catalytic activity for a number of reactions, including the OER. However, the exposure of the active sites on layered double hydroxides (LDHs) is hindered by their stacking structure. Exfoliation is an efficient approach to address the above issue. Wang and co-workers developed two effective liquid-phase and gas-phase exfoliation methods with the assistance of plasma, focusing on enhancing the catalytic OER activities of CoFe LDHs nanosheets.[78] The water-plasma-coupled exfoliation method was applied on CoFe LDHs nanosheets, yielding ultrathin CoFe LDHs nanosheets with highly-exposed active sites and massive defects and vacancies, which in turn leads to outstanding catalytic activity for the OER (overpotential of 232 mV at 10 mA cm^{-2} and a Tafel slope of 36 mV dec^{-1}). As well acknowledged and demonstrated in the previous sections, Fe-incorporation in OER catalysts can remarkably boost their unsatisfactory catalytic activity. For example, Lou and co-workers first synthesized nanoprisms of a Ni precursor as the self-sacrificing

templates, which was consumed under the environment of $FeSO_4$ hydrolysis and simultaneously formed Ni-Fe LDH nanosheets (Figure 5E).[36] As shown by the HAADF-STEM image in Figure 5F, the hierarchical hollow nanoprism is consisted of interconnected, highly porous, and loosely packed Ni-Fe LDH nanosheets. The hierarchical Ni-Fe LDH electrocatalyst exhibits a small overpotential of 280 mV at 10 mA cm^{-2} for OER (Figure 5G), indicating excellent catalytic activity for the OER.

As evidenced by many reported works, the hydroxide and oxide structures would transform into oxyhydroxides during the OER process.[79] Thus, the syntheses and applications of earth-abundant oxyhydroxide electrocatalysts for the OER are of great interest. The active sites of the OER are usually related to cations with high valence states (or oxidation states), such as Fe^{3+}, Fe^{4+}, Co^{3+}, Co^{4+}, and Mn^{3+}, rather than their divalent counterparts. The high valence cations may serve as an electron acceptor, which digests the generated electrons and hence facilitate the reaction to proceed to the product side ($M^{n+1} + e^- \rightarrow M^{n+}$). The Fe species plays a crucial role in enhancing the activity of Co- and Ni-based oxyhydroxide OER electrocatalysts. Using DFT calculations and the *operando* XAS technology, Enman *et al*. pointed out that the Fe element doped in the CoFe oxyhydroxide (CoFeOOH) catalyst is partially oxidized and the Fe-O bond is shortened under OER operating conditions. The results further evidence that the OER mainly takes place on Fe-based active sites.[34] The incorporation of the third metal, such as W and V, into CoFeOOH further enhances the catalytic performance. The adsorption energies of the OER intermediates (*OOH, *OH, and *O) are crucial descriptors to predict and examine the OER activity of the catalysts. Using DFT calculations, Zhang *et al*. demonstrated that Fe and W co-doped Co oxyhydroxide gives a near-optimal OH adsorption energetics, which theoretically in turn exhibits significantly enhanced catalytic activity towards OER. Inspired by the DFT predictions, they used a sol-gel approach to fabricate FeCoW ternary

oxyhydroxide catalysts with homogeneously distributed metal atoms.[35] The optimized geometrical (amorphous phase and compressive strain induced by larger W atoms) and modulated 3d electronic structures of the catalysts were found accountable for the enhanced intrinsic activity for the OER. The FeCoW oxyhydroxide electrocatalyst outperforms other catalysts with a low overpotential of 223 mV at 10 mA cm^{-2} on a glassy carbon electrode without iR compensations and conductive carbon additives. NiFe oxyhydroxides are probably the most active OER catalysts in alkaline conditions. Research attentions have been attracted to unravel the fascinating mysteries behind such high activities. For example, Boettcher and co-workers emphasized that the incorporated Fe at the defects and edges sites of NiFe oxyhydroxide catalysts contribute more to the enhanced activity comparing with Fe doped in the bulk.[80]

3.4 Chalcogenides

Non-noble-metal chalcogenides (mainly sulfides and selenides) have attracted numerous research attentions in application to the OER. The most commonly used methods reported so far to fabricate metal sulfide and selenide structures are solvothermal and thermochemical treatment. For the solvothermal method, the common sulfide sources are thiourea and thioacetamide, *etc.*, while the usually used selenide sources are selenourea, sodium selenide, and sodium hydrogen selenide, *etc.* The widely used sulfur and selenium sources for the thermochemical treatment are sulfur and selenium powders. Hierarchical bimetallic NiFeS electrocatalyst was reported by Xuan *et al*. via a hydrothermal sulfurization reaction and a following post-annealing treatment on NiFe-based PBA precursors.[81] The NiFeS catalyst with a sea urchin-like morphology shows an ultralow overpotential of 200 mV at 10 mA cm^{-2}, benefiting from the enhanced electrical conductivity, the complex valence states, the efficient mass transfer, and the exposure of abundant active sites. As highlighted by Wen

and co-workers, amorphous Co sulfide porous nanocubes (A-$CoS_{4.6}O_{0.6}$ PNCs) were fabricated by the ionic exchange reaction on CoFe PBA with Na_2S replacing $[Fe(CN)_6]^{3-}$ (**Figure 6**A-B).[38] The A-$CoS_{4.6}O_{0.6}$ PNCs show excellent catalytic activity towards the OER, which greatly outperforms bulk CoS_2 and is comparable to that of the state-of-the-art RuO_2 catalyst (Figure 6C). The adsorption of *O intermediate in OER is optimized by the incorporation of heteroatom O and the Co-S dangling bonds, which is highly responsible for the enhanced catalytic OER activity. Non-noble-metal-based selenides were also evidenced to be effective OER electrocatalysts. For instance, Nai *et al*. firstly fabricated Ni-Fe PBA nanocages via a site-selective ammonia etching process on the Ni-Fe PBA nanocube precursors.[40] As shown in Figure 6D-H, the ammonia etching time plays a crucial role along the morphology evolution process from nanocube to nanocage structures. Then the Ni-Fe PBA nanocages were transformed to Ni-Fe diselenide nanocages via a selenization treatment. Benefited from its unique open and hollow structure, the enhanced electrical conductivity, and the modulated electronic structure by incorporating Se, the as-prepared Ni-Fe diselenide nanocage electrocatalyst exhibits outstanding OER performance with a low overpotential of 240 mV to obtain the current density of 10 mA cm^{-2} and a small Tafel slope of 24 mV dec^{-1}, which greatly outperforms Ni-Fe-Se with other structures and the corresponding Ni-Fe PBA (Figure 6I-J).

3.5 Phosphides

Non-precious metal (mainly Fe, Co, and Ni) phosphides with varying morphologies and compositions have been widely investigated recently owing to their outstanding performance for the OER. Derived from Ni-Ni PBA nanoplates, Yu *et al*. prepared NiP, NiO, and $Ni(OH)_2$ nanoplates via varying treatment methods, such as phosphorization reaction, thermal annealing, and chemical etching (**Figure 7**A).[82] A representative TEM image shown in Figure 7B demonstrates the rough and porous feature

of the NiP nanoplate. The NiP nanoplate catalyst coated with porous carbon materials shows excellent catalytic activity for OER, outperforming NiO and $Ni(OH)_2$ nanoplates recorded in 1.0 M KOH solution (Figure 7C). Starting from another MOF material, *i.e.*, ZIF-67 nanocube, He *et al*. fabricated carbon incorporated Ni-Co phosphide (Ni-Co-P) nanoboxes by hydrothermal and phosphorization reactions.[44] The incorporated amorphous carbon materials derived from the organic ligands in ZIF-67 greatly enhance the electrical conductivity and the electrocatalytic activity for the OER of the Ni-Co-P nanoboxes. Later, Hu *et al*. fabricated Ni-Co-P hollow nanobricks (HNBs) through a template-assisted method followed by thermal annealing, chemical etching, and phosphorization processes (Figure 7D).[43] The unique hierarchically hollow architectures of the as-prepared Ni-Co-P nanobricks enable highly exposed active surface area and improved mass diffusion efficiency, endowing the Ni-Co-P nanobrick catalyst remarkable activities toward OER in 1.0 M KOH solution (Figure 7E).

The metal phosphide materials prefer to transform into metal oxyphosphide structures during the OER process. Recently, Zhang *et al*. synthesized hollow Co-Fe phosphide (Fe-Co-P) nanoboxes by a phosphorization treatment on the as-prepared FeCo PBA nanoboxes, then the phosphorus atoms were substituted by oxygen atoms in the OER operating conditions, yielding metal oxyphosphide structures (Figure 7F-G).[83] A low overpotential of 269 mV to drive a current density of 10 mA cm^{-2} is obtained on the Fe-Co-P nanobox electrocatalyst in 1.0 M KOH solution (Figure 7H), which can be attributed to the merit of the porous hollow structure and the intermolecular electronic coupling effect between Fe and Co atoms through P/O bridges. The directly obtained non-noble-metal oxyphosphide materials are also widely reported recently. The multimetallic oxyphosphide particles with multishells were prepared by Guan *et al*. via a consecutive thermochemical treatment and phosphidation reaction on mixed-metal coordination polymer precursors (Figure 7I).[84] As shown by the field emission scanning

electron microscopy (FESEM) (Figure 7J) and the TEM images (Figure 7K-L), the particles exhibit a clearly seven-layer structure consisting of small nanocrystal pieces in each layer. This strategy can be universally applied on other metals with varying combinations and compositions (such as MnCo, NiCo, NiMn, and MnNiCo). The Mn-Co oxyphosphide catalysts were electrochemically activated to transform into oxides and hydroxides, which exhibit appreciable activities and stabilities toward the OER and outperform the as-prepared Mn-Co oxyphosphide as well as the Mn-Co oxide in 1.0 M KOH solution (Figure 7M). Recently, Zhang *et al*. synthesized CoFe oxyphosphide microtubes via a readily self-templated strategy.[5] The Fe-based metal-organic compound microrod precursors were firstly synthesized, followed by a hydrothermal reaction to yield CoFe LDH microtubes and then a phosphorization treatment to fabricate CoFe oxyphosphides. The obtained CoFe oxyphosphide electrocatalyst processes hierarchically hollow structures and strong intermetallic synergistic effect, endowing them outstanding catalytic performance for both OER and HER.

The (oxy)phosphides will be easily oxidized to oxides/hydroxides under harsh OER operating conditions. An open question is: why not to design OER catalysts directly in the form of oxide or (oxy)hydroxide? The doping of heteroatoms, such as phosphorus, sulfur, selenium, *etc.*, usually with a lower electronegativity comparing with that of oxygen, would optimize the electronic structure of the OER catalyst, affect the adsorption energies of the OER intermediates, and finally enhance their activities. Although the heteroatom dopants in the catalysts are not stable during the OER electrochemical process, those heteroatoms underneath the reactive surface layer (transformed into oxide/hydroxide) can survive and contribute significantly to facilitate the OER kinetics even at a low content.

Inspired by the appreciably enhanced catalytic activity by the heteroatom (*e.g.*, S, P, and Se)

doping strategy, researchers have made great efforts to combining two heteroatom dopants to form metal phosphosulfides or phosphoselenides.[85,86] It is acknowledged that non-noble-metal phosphosulfides are excellent candidates to catalyze HER.[87] There are some typical non-noble-metal-based phosphosulfide electrocatalysts (such as CoPS, NiPS, NiFePS, *etc.*) for the OER. For example, Song *et al*. synthesized NiFe phosphosulfide nanosheets as bifunctional catalysts for OER and HER.[88] The controlled amount of Fe incorporated in $NiPS_3$ into the bimetallic $NiFePS_3$ catalyst enables the enhanced electrical conductivity, finely tuned electronic structure, and hence remarkable catalytic activities for OER and HER. Interestingly, the authors also suggest that the formed NiFe hydroxide and oxyhydroxide under OER operating conditions may be the true active species for the OER.

3.6 Phosphates/borates

The electrocatalytic performance of OER electrocatalysts is highly dependent on the pH value of the electrolyte. Eco-friendly electrolyte, such as potassium borate in nearly neutral pH, is of paramount importance to address the serious environmental suffering and equipment corrosion at extreme pH conditions. Non-noble-metal-based phosphates and borates catalysts show remarkably catalytic activities for the OER, particularly in alkaline and neutral media. In 2008, Kanan and Nocera reported an electrodeposited, durable, and self-healing Co phosphate (Co-Pi) film catalyst with the capability to work in neutral media.[19] Since then, non-noble-metal phosphates have attracted tremendous research attention. Xie *et al*. reported a Co-Pi nanoarray catalyst on Ti mesh via the oxidative polarization reaction on Co phosphide in a phosphate-buffered solution.[21] Attributed from the unique three-dimensional nanoarray morphology, the as-obtained Co-Pi nanoarray catalyst enables the exposure of abundant active sites and the enhanced charge and mass transfer efficiencies, resulting in

a low overpotential of 450 mV at 10 mA cm^{-2} in a phosphate-buffered solution. Using a non-aqueous sol-gel microwave irradiation synthesis method, Gershinsky and Zitoun prepared $LiCoFePO_4$ olivine coated with reduced graphene oxide as a hybrid material for OER, which exhibits an overpotential of 390 mV at 5 mA cm^{-2}.[89] Co/Fe-based borates are another group of emerging efficient OER electrocatalysts in neutral media. Ren *et al*. fabricated a Co borate (Co-Bi) nanoarray electrocatalyst on Ti mesh via a facile topotactic electrochemical conversion of Co diselenide nanoarray, which displays a low overpotential of 420 mV at 10 mA cm^{-2} and excellent stability for the OER under benign conditions.[45] Chen *et al*. prepared a hybrid material consisting of strongly coupled ultrathin Co-Bi nanosheets and graphene host, which exhibits a low overpotential of 290 mV at 10 mA cm^{-2} and a small onset potential of 235 mV in alkaline and neutral media.[20]

3.7 Other compounds

In addition to the above mentioned non-noble-metal-based catalytic materials, other earth abundant metal-based compounds such as borides,[47,90,91] nitrides,[48,49,92] cyanides,[93] and chlorides,[51] have also been proven to be efficient electrocatalysts for the OER. Recently, Nsanzimana *et al*. highlighted an amorphous ternary metallic boride (Fe-Co-2.3Ni-B) electrocatalyst synthesized via a facile chemical reduction strategy.[90] A clearly amorphous thin metal oxide/borate layer can be observed on the metal boride particles. The Fe-Co-2.3Ni-B catalyst shows appreciable catalytic activity (overpotential of 274 mV at 10 mA cm^{-2} and Tafel slope of 38 mV dec^{-1}) for the OER in alkaline media, outperforming those of the binary and unary metallic borides as well as the state-of-the-art Ir/C electrocatalysts. The activities of the OER electrocatalysts are often deteriorated by their poor electrical conductivities. Transition metal nitrides might be able to address this issue in view of their extraordinarily high intrinsic conductivities. Driess and co-workers fabricated crystalline manganese

nitride on Ni foam (Mn_3N_2/NF) via the electrophoretic deposition method, which displays a low overpotential of 270 mV for achieving a current density of 10 mA cm^{-2} and excellent durability with nearly no activity decay after the one-week test.[48] The Mn_3N_2/NF catalyst with the intimate connection between the reactive MnO_x layer and the metallic Mn_3N_2 endows high electrical conductivity and hence remarkable catalytic activity for the OER. In addition, MOFs, as a class of functional materials and precursors, along with their derivatives and composites, serve as a group of promising OER electrocatalysts attributed to the compositional and structural diversities, porous structure with controllable pore size, highly exposed surface area, highly crystalline property, and surface functionality.[22,44,94]

So far, a wide range of noble-metal-free OER electrocatalysts has been evaluated with varying OER performance (**Table 1**). Non-noble-metal-based metals and alloys usually need to be stabilized by hosts (*e.g.*, carbon materials) or saturated with high electronegativity elements since they cannot survive directly in harsh acidic and alkaline media. Earth-abundant metal oxides and (oxy)hydroxides have been widely studied, which exhibit appreciable OER performance and are considered as a group of very promising candidates for OER electrocatalysts. Recently, non-noble-metal chalcogenides and pnictides have received more and more research attention as OER electrocatalysts due to their significantly improved electrocatalytic performance through heteroatom doping. In addition, non-noble-metal-based phosphates and borates were also found capable of catalyzing the OER in alkaline media and even in benign neutral media with good performance. Notably, the OER is operated under strong oxidative environment involving lots of strong oxidizing intermediates (*e.g.*, O, OH, and OOH). Most of the non-noble-metal-based OER electrocatalysts, such as oxides, hydroxides, chalcogenides, and pnictides, tend to transform into oxyhydroxides on the catalyst surface during the

OER process.[79] Moreover, among all non-noble-metal-based electrocatalysts, noble-metal-free oxyhydroxides (*e.g.*, NiFe oxyhydroxides and FeCoW oxyhydroxides) are perhaps the most active, stable, and promising OER electrocatalysts reported so far.[35] However, the real active centers for the OER are still under debate and need further explorations. Noble-metal-free OER electrocatalysts usually show excellent performance in alkaline media but cannot work efficiently in acidic solutions. Great efforts have been devoted to address this major technological challenge. For example, some non-noble-metal-based materials were shown to exhibit good OER performance in acidic solution, such as Co-containing polyoxometalates,[95] MnO_x,[96] Ti-stabilized MnO_2,[97] and iron oxide embedded titania nanowires.[98] Thanks to the tremendous research efforts made in the past decades, a great scientific stride has been achieved in the field of non-noble-metal-based OER electrocatalysts. However, their electrocatalytic performance is still relatively low and cannot fulfill the promise of large-scale commercialization. Many effective strategies have been developed to improve the performance of OER electrocatalysts. Besides improving the intrinsic activity, which can be boosted by harnessing the synergistic effect via alloying or heteroatom doping, increasing the number of active sites through incorporating high specific surface area support, and designing nanostructures for electrodes are also effective strategies.[17,36,40] In addition, combining materials with different functions to form nanocomposites is also an efficient strategy to fabricate OER electrocatalysts with appreciable performance.[22,67] At present, it remains a difficult task to enhance the OER performance of non-noble metal based electrocatalysts for the large-scale commercialization.

4. Reaction mechanisms

As stated above, a vast body of non-noble-metal-based OER electrocatalysts has been reported so far. While many researchers claimed that they had developed earth-abundant catalysts outperforming the

commercial noble metal catalysts mostly based on the obtained overpotentials, few of them have made a real breakthrough to further overcome the high overpotential, promote the process of the mass commercialization, and substitute the noble-metal-based catalysts ultimately. The research attention of the OER electrocatalysts mainly reflects in the material design and development, structural characterization, and catalytic performance optimization. However, the understanding of the reaction mechanism for the OER is of great importance to guide and hence improve the catalyst design. The reaction mechanism of OER remains elusive with lots of open questions. To name a few, what is the active site? Are all metal atoms catalytically active? How does the structure of the catalysts change during OER operation? These tough questions still remain unsolved due to the short life of the catalytically active transient states, the limitation of the experimental techniques to capture information at the dynamically atomic level, as well as the currently restricted computational methods to deal with complicated systems. In this section, based on the current knowledge of the reaction mechanism for the OER, we briefly discuss the reaction pathways, the thermodynamic scaling relation, and the activity descriptors of the OER.

4.1 Reaction pathways

From the theoretical calculation perspective, the following four-step reaction pathway in acidic condition has been proposed by Nørskov as described by Equations (5-8):[53]

$$H_2O + * \rightleftharpoons *OH + (H^+ + e^-) \quad (5)$$

$$*OH \rightleftarrows *O + (H^+ + e^-) \quad (6)$$

$$*O + H_2O \rightleftarrows *OOH + (H^+ + e^-) \quad (7)$$

$$*OOH \rightleftarrows O_2 + (H^+ + e^-) + * \quad (8)$$

In alkaline media, the reaction pathway is shown by Equations (9-12):

$$OH^- + * \rightleftarrows *OH + e^- \quad (9)$$

$$*OH + OH^- \rightleftarrows *O + H_2O + e^- \quad (10)$$

$$*O + OH^- \rightleftarrows *OOH + e^- \quad (11)$$

$$*OOH + OH^- \rightleftarrows O_2 + H_2O + e^- + * \quad (12)$$

The asterisk (*) in the equations denotes an active site or a bond to the surface. It is worth mentioning that there are lots of different reaction pathways proposed by researchers, arguing that the dynamic OER process does not necessarily go through the above pathways. Most of them are debating where the adsorbed O species (*O) and the final product O_2 come from. For example, *O can be generated by Equation (13) while O_2 may be formed by coupling two *O species directly in Equation (14):[99]

$$*OH + *OH \rightleftarrows *O + H_2O + * \quad (13)$$

$$*O + *O \rightleftarrows O_2 + 2* \quad (14)$$

We note here the by-product hydrogen peroxide may be produced by Equation (15) in a weaker oxidation environment:[100,101]

$$*OH + *OH \rightleftarrows H_2O_2 + 2* \quad (15)$$

4.2 Thermodynamic scaling relation

As displayed in the above OER reaction pathways, *O, *OH, and *OOH are three most important intermediates evolved in the OER process. It is desperately needed to unravel the relationships between those intermediates and the origin of the overpotential for the OER at the theoretically atomic level. There are some linear relationships among the binding energies of different intermediates. Based on a database of diverse oxide catalyst models, a scaling relation, where an approximate constant difference of 3.2 eV between the binding energies of *OH and *OOH, was proposed by

computational scientists.[53] In other words, the binding energies of the adsorbed *OH and *OOH intermediates show a linear correlation with an intercept of 3.2 eV regardless of the catalysts (**Figure 8**A). The nature of this linear correlation originates from the similar adsorption configurations of *OH and *OOH via a single O-M (M denotes the surface) bond.[53]

According to the computational hydrogen electrode,[102] the ideal free energy diagram of the OER is plotted in Figure 8B. When the corresponding intermediates involved in the OER process locate at the ideal position in the free energy diagram, *i.e.*, a free energy gap of 1.23 eV is shown between every pairs of neighboring adsorbates in Figure 8B, this ideal OER electrocatalyst exhibits zero overpotential. However, in reality, the bindings of the reaction intermediates always differ from the ideal case. The OER overpotential is determined by the RDS, which is often reported as the second (the formation of *O) or the third (the formation of *OOH) steps.[53] According to the scaling relation, the constant difference between the binding energies of *OH and *OOH can be converted to the overpotential via (3.2 – 2.46) eV/2e, giving a minimum overpotential of 0.2-0.4 V with a requirement of a moderately adsorbed *O in the middle of *OH and *OOH in the energy diagram.[53] The trends of the overpotentials obtained from both calculations and experiments fit well.[53,103,104] This constitutes a major reason why the most reported experimental OER overpotentials locate in a narrow range of 0.2-0.4 V. Unfortunately, no reported examples so far have broken the scaling relations. The experimentally obtained enhanced OER activity (mostly claimed via negatively shifted overpotentials at a specific current density) by increasing the loading or surface area does not mean the breaking of the scaling relations.[105] Of course, the experiments are usually complex considering lots of impacting factors. For example, the catalytic performance of the catalysts for the OER is dependent on the conductivity of the electrode, the dispersity of the tested catalysts, the resistance and the

corresponding compensation method. In addition, the experimental overpotential strongly depends on the current density value, whereas there is no reflection in the theoretically calculated one.[53] Nonetheless, one can manipulate the adsorption energies of the key intermediates on the rationally designed catalyst to overcome the restricted relationships. First, even the scaling relation is universally true, the binding energy of *O on the catalyst should be in the middle of *OH and *OOH species as much as possible. Then, to break the scaling relation, one must seek catalysts that can stabilize the adsorption of *OOH relative to *OH. The synergistic effect of using multi-metallic-based, heteroatom-doped, and support/substrate-modified catalysts could achieve the optimized adsorptions. The fine tuning of the atomic and electronic structure assisted by theoretical inputs is the ongoing work. The Gibbs free energy diagram is a practical and effective tool for the screening, testing and predicting of the materials for applications in multiple reactions, such as OER, ORR and HER.[53,102] However, the kinetic barriers, *i.e.*, the elementary step barriers obtained from the transition states, have not been considered in the mechanistic studies.[3] The overpotentials from theoretical calculations are hence underestimated and cannot precisely reflect the nature of the reaction mechanism.

4.3 Activity descriptors

The chemical reactions of OER and ORR are very complicated with several elementary reactions and a large amount of intermediates involved. The finding of an appropriate descriptor which usually presents in a volcano-shaped relationship, therefore, is greatly needed.[106] Based on the scaling relation and the RDS of OER, the theoretical overpotential is highly dependent on the free energy difference between ΔG^{o}_{*O} and ΔG^{o}_{*OH}, which is translated to a volcano plot (Figure 8C) by Rossmeisl and co-workers. A group of oxide OER catalysts was calculated and plotted in Figure 8C, exhibiting a

volcano shape where the Co_3O_4 and RuO_2 catalysts with the lowest OER overpotentials located at the summit. At the peak region of the volcano plot, the Gibbs free energy gap between *O and *OH is approximately 1.6 eV, which coincides with the scaling relation mentioned above where the adsorption energy of *O locates in the middle of those for *OH and *OOH in the free energy diagram. The descriptor of $\Delta G^{o}_{*O} - \Delta G^{o}_{*OH}$ is easy to be calculated and hence can be utilized to effectively seek and predict OER catalysts computationally. In principle, the binding energies of the adsorbates can be changed by modulating the surface electronic structure of the catalyst,[107] for instance, the e_g filling of the surface transition metals as proposed by Shao-Horn and co-workers.[108] In Figure 8D, a volcano plot between the OER overpotential and the e_g electron filling is shown, where $Ba_{0.5}Sr_{0.5}Co_{0.8}Fe_{0.2}O_{3-\delta}$ with the highest OER catalytic activity locates at the summit. The e_g occupation is strongly related to the binding energies of the surface oxygen, which follows the Sabatier principle that the binding between the adsorbate and the catalysts should be neither too weak nor too strong.[106] This OER activity descriptor provides a powerful approach to examine or predict perovskite oxide OER catalysts from the molecular orbital principle level.[108] Other OER activity descriptors aiming to simplify the complicated reaction pathway were proposed by other researchers, including the enthalpy change of a lower to higher oxide transition by Trasatti,[109] the 3d electron number of bulk transition metal ions by Bockris and Otagawa,[103] and the M-OH bond strength by Markovic and co-workers.[104] More efforts should be devoted to develop more accurate descriptors in the future.

5. Practical applications

5.1 Water splitting

Water electrolysis can provide CO_2-free hydrogen for energy storage and chemical synthesis which is crucial for enabling increased solar energy capacity and CO_2 utilization technologies.[110,111] Using a bifunctional electrocatalyst towards OER and HER has advantages of simplifying the system and lowering the cost. The alkaline water electrolysis plays an important role in the chemical industry, which utilizes earth-abundant metals as the electrode materials and sometimes shows competitive or even better efficiency than noble-metal-based electrocatalysts operated under acidic water electrolysis.[112] It is thus highly attractive to make a noble-metal-free bifunctional electrocatalyst efficient for both OER and HER in strongly basic media. Hu *et al*. developed hierarchical Ni-Co-P hollow nanobricks (HNBs) with high efficiency for the overall water splitting.[43] The Ni-Co-P electrocatalyst exhibits low overpotentials of 270 mV and 107 mV to drive a current density of 10 mA cm^{-2} for OER and HER in alkaline media, respectively. When the Ni-Co-P nanoarchitecture is used simultaneously as the cathodic and the anodic electrocatalysts, an ultralow cell voltage of only 1.62 V is needed to achieve the current density of 10 mA cm^{-2} (**Figure 9**A). This highly efficient electrocatalyst also shows remarkable durability for overall water splitting with only a 6.6% current loss over 20 h at a cell potential of 1.62 V (Figure 9B). Later, Zhang *et al*. fabricated unique CoFe oxyphosphide microtubes as the electrocatalyst for the overall water splitting.[5] The CoFe oxyphosphides display overpotentials of 280 mV and 180 mV for OER and HER, respectively, as well as a cell voltage of 1.69 V for overall water splitting to reach the current density of 10 mA cm^{-2} (Figure 9C). Bimetallic NiFe phosphosulfide nanocomposite also exhibits appreciable overall water splitting performance with a low cell voltage of 1.58 V to achieve the current density of 10 mA cm^{-2}.[113] Moreover, nanoengineering active edge sites and interfacial catalysis are effective strategies to enhance the intrinsic activity of catalytic materials, as proven in both OER and HER.[114-116]

Introducing more edges and corner sites helps decrease the coordination number of the surface reactive sites and affects the electronic structure of catalysts, which in turn boost the electrocatalytic performance.[114,116] Despite the current progress made in the subject of the alkaline overall water splitting, the current working efficiency of the water electrolyzer is still very low and more efforts should be devoted. Comparing with alkaline electrolyzers, acidic proton exchange membrane electrolyzers afford much higher hydrogen generation rates.[117] However, earth-abundant metal electrocatalysts are unstable in acidic media. Currently, efficient electrocatalysts for acidic water oxidation are mainly noble-metal-based materials.[118,119] The development of effective non-noble-metal-based OER and HER electrocatalysts under acidic condition should receive more research attention in the future.

5.2 Metal-air batteries

Metal-air batteries are one of the most promising electrochemical energy storage devices in applications to portable devices, electrical vehicles, and the large-scale grid storage. Among all metal-air batteries, including zinc, aluminum, magnesium, and lithium metals with negative electrode potentials refer to the standard hydrogen electrode, Zn-air battery (ZAB) is the most promising one owing to its high theoretical energy density, environmental amity, affordable price, and high-level safety. Two key electrochemical reactions, *i.e.*, OER and ORR, take place during charging and discharging operation processes of a metal-air battery. However, the research progress and the commercialization of the metal-air batteries are greatly hindered by the sluggish kinetics and the lack of efficient bifunctional electrocatalysts for OER and ORR. The rational design and development of non-noble-metal-based, highly active, and durable bifunctional electrocatalysts for both OER and ORR is urgently needed for applications in rechargeable metal-air batteries. Recently, Lu *et al*.

engineered MnO and Co species with massive heterointerfaces into the porous graphitic carbon (MnO/Co/PGC) as a hybrid nanocomposite through a readily hydrothermal and post-annealing strategy derived from a bimetal-organic framework precursor.[6] The MnO/Co/PGC nanocomposite is capable to catalyze both OER and ORR with high efficiencies. When it is used as an efficient air cathode in a home-made rechargeable ZAB (Figure 9D), a high peak power density of 172 mW cm^{-2} (Figure 9E) and a remarkable operating durability up to 350 cycles (Figure 9F) are offered, outperforming the mixture of the commercially available Pt/C and RuO_2 catalysts. Zhang *et al*. reported a hierarchical rod-like electrocatalyst with uniformly distributed Co NPs encapsulated by N-doped carbon rings via a facile carbonization method on the corresponding MOFs material.[7] The hybrid electrocatalyst displays appreciably high catalytic activity for both OER and ORR. The rechargeable ZAB based on this hybrid electrocatalyst provides initial charge and discharge potentials at 1.81 and 1.28 V at 2 mA cm^{-2}, respectively, together with a remarkable durability showing no polarization increase after 300 cycles. The ZAB is capable of powering a water-splitting device using the same hybrid electrocatalyst to catalyze OER and shows high working efficiency.

5.3 Reversible fuel cells

The reversible fuel cell (RFC), which can produce hydrogen fuel via electrocatalysis using electricity, is similar to the rechargeable battery.[120] A RFC requires efficient bifunctional electrocatalysts for both OER in the electrolyzer mode and ORR in the fuel cell mode. OER, as an uphill chemical reaction with sluggish reaction kinetics, serves as a major obstacle for the development of this technology. Normally, a bifunctional electrocatalyst for both OER and ORR is usually hard to achieve simultaneously owing to the very different characteristics of the catalysts required by the reactions. The integration of two functionalities (OER and ORR for RFC and rechargeable metal-air batteries,

OER and HER for water electrolysis) into one bifunctional composite is urgently needed, which would simplify the design of the energy storage/conversion devices, increase the power-to-weight ratio, and enhance the working efficiency and portability. Strasser and co-workers reported a bifunctional electrocatalyst which integrates the OER reactive Ni-Fe LDH and the Fe-N-C ORR catalyst by a simple physical mixing method.[8] This bifunctional catalyst displays an unprecedentedly low combined OER (at 10 mA cm^{-2}) and ORR (at -3 mA cm^{-2}) overpotential of 0.747 V in alkaline condition. The further anion exchange membrane electrode assembly tests in a unitized fuel cell/electrolyzer cell confirm the remarkable catalytic performance of the bifunctional catalyst, outperforming that of the noble metal catalysts.

6. Conclusion and perspectives

This review has introduced some evaluation criteria for the OER and outlined the recent advances in the innovation and development of non-noble-metal-based OER electrocatalysts. A wide range of earth-abundant electrocatalysts, including metals/alloys, oxides, hydroxides, phosphides, sulfides, selenides, phosphates/borates, *etc.*, as well as their hybrids, exhibit appreciable OER performance. Thankfully, some OER electrocatalysts have manifested excellent catalytic activity (overpotential < 300 mV at 10 mA cm^{-2}) and stability (negligible decay after tens of hours or thousands of cycles) towards OER, especially in alkaline media. The current understanding of the reaction mechanisms for the OER has also been discussed, providing some atomic-level insights for the future rational design of OER electrocatalysts. The research progresses of the practical applications of OER, including water electrolysis, metal-air batteries, and reversible fuel cells, show a huge stride towards the clean and sustainable energy society. In general, although delightful scientific achievements have been reported, there are still many challenges to be overcome and much room to be explored in this field. Besides the

intractable challenges, some possible solutions, perspectives and future directions to address the corresponding challenges are also provided as follows.

(1) The electrocatalytic OER performance can be affected by lots of factors, including catalyst loadings, electrolytes, supporting substrates, morphology of materials, and electrochemical measurement methods. Standard evaluation protocols of the OER performance are lacking. A benchmarking methodology or an impartial third party to objectively evaluate the OER performance of the electrocatalysts should be greatly encouraged. This will provide opportunities in comparisons of the performance for OER electrocatalysts from different groups and institutes in a fair manner.[121,122]

(2) The unsatisfactory intrinsic activity and the limited exposure of the electrochemical active sites for the non-noble-metal-based OER electrocatalysts greatly hinder their wide application in practical devices. Research efforts to emphasizing activity record by increasing catalyst loading should be avoided.[105] Instead, future research attention should concentrate more on boosting the intrinsic activity of non-precious OER electrocatalysts. The intrinsic activity for OER is strongly related to the electronic structure (especially d-electron) of the active atoms, which can be tuned by doping with other metals and heteroatoms. The doping strategy enables the synergistic effect, which intrinsically correlates with the optimized electronic structures originating from the electronegativity discrepancy between different elements. More intuitively, the tuning of the valence states on the reactive species is crucial to enhance the intrinsic OER activity. From the theoretical perspective, the intrinsic activity of the OER can be tuned by optimizing adsorption configurations of OER intermediates. As suggested by the Sabatier principle, the adsorption of the intermediates should be neither too week nor too strong.[106] The nature of the optimized adsorptions originates from the modulated electronic structures of the catalysts. In addition, the construction of catalytic materials into

hierarchically three-dimensional morphologies,[36,72] the incorporation of supports with high specific surface areas,[27,67] and the preparation of small nanoclusters and single-atom catalysts[65] are effective strategies to efficiently expose the active sites.

(3) Although numerous non-noble-metal-based OER electrocatalysts have been developed via diverse methods in the past decades, there is still a long way to go to realize the mass commercialization of OER electrocatalysts in practical devices. Exploring new materials as idea non-noble-metal-based OER electrocatalysts is the most essential focus in the near future. The new materials should overcome the previously mentioned challenges as much as possible and meet the following standards: (a) low cost including the synthetic raw material and the fabrication process; (b) extraordinary catalytic OER activity outperforming the state-of-the-art commercial electrocatalysts; (c) robust stability which can effectively operate in a commercialized device for a few years; (d) capability to catalyze OER at a wide range of pH values, especially under acidic media and eco-friendly neutral electrolytes; (e) scaling up capability for the mass commercialization.[121] However, none of the OER electrocatalysts reported so far have satisfied the above merits together. More efforts hence should be afforded in the future.

(4) The intrinsic active sites and the reaction mechanism for the OER remain elusive, especially from the comprehensively theoretical calculations. The development of efficient OER catalysts still strongly depends on the experimental trial and error. Hence, in-depth and systematical theoretical investigations should be encouragingly incorporated into the material design and fabrication processes of OER catalysts. Simple and accurate descriptors from theoretical predictions and examinations of OER activity and stability are greatly needed.[108] The calculations of the kinetic reaction barriers should also be included to obtain more accurate results.[123]

(5) Currently, most of the reported works are based on *ex situ* techniques, which only give the characterization results of OER catalysts before and after electrochemical measurements but cannot provide the structural evolution information during the OER process. Therefore, *in situ* techniques are desirable for characterizing the structure-activity relationships of the catalysts.[124,125] The combination of *in situ* techniques, theoretical calculation approaches, and the electrochemical measurements is an effective strategy to unravel the reaction mechanism and hence guide the rational design of efficient OER electrocatalysts.

(6) Currently, most of the reported non-noble-metal-based OER electrocatalysts are evaluated in alkaline conditions. The operation of the OER in alkaline solution requires a gas separation unit along with the decreased pH value which needs to be overcome by the replenishment of the alkaline electrolyte. The alkaline electrolyte also excludes their applications in proton exchange membrane electrolyzers. The design of earth-abundant OER electrocatalysts in acidic media can be achieved by protecting OER active centers through structurally stable elements (*e.g.*, Mn oxides and perovskites).[126]

(7) The electrochemical OER process involves multi-electron transfer. The OER performance is hence highly dependent on the conductivity of the materials. In fact, catalytic materials with highly active sites but low conductivity may show poor overall catalytic performance. The construction of the efficient charge transfer network via the rational design of unique morphologies, the incorporation of highly conductive carbon materials and metallic frameworks, and the strong coupling between the reactive species and the conductive host are effective approaches to improve the conductivity of the electrocatalysts.[20,27]

(8) The lack of efficient bifunctional electrocatalysts greatly hinders their practical applications

in the water electrolysis (requires OER and HER bifunctional electrocatalysts), metal-air batteries and reversible fuel cells (both need OER and ORR bifunctional electrocatalysts). Integrating two functional materials by *in situ* growth and post-treatment or even by simply physical mixing to fabricate bifunctional materials can simplify the design of the energy storage/conversion devices, increase the power-to-weight ratio, and enhance the working efficiency and portability.[8]

In conclusion, in the past few decades, a huge stride has been achieved in the development of the non-noble-metal-based OER electrocatalysts, which serve as potential alternatives of noble metal catalysts. This review provides some recent advances of the non-noble-metal-based OER electrocatalysts and offers some perspectives for future developments.

Acknowledgements

X.W. Lou acknowledges the funding support from the National Research Foundation (NRF) of Singapore via the NRF Investigatorship (NRF-NRFI2016-04). S.Q. Zang acknowledges the funding support from the National Science Fund for Distinguished Young Scholars (21825106) and the National Natural Science Foundation of China (No. 21671175).

References

[1] S. Chu, A. Majumdar, *Nature* **2012**, *488*, 294.

[2] Y. Jiao, Y. Zheng, M. Jaroniec, S. Z. Qiao, *Chem. Soc. Rev.* **2015**, *44*, 2060.

[3] T. Reier, H. N. Nong, D. Teschner, R. Schlögl, P. Strasser, *Adv. Energy Mater.* **2017**, *7*, 1601275.

[4] P. Zhang, L. Yu, X. W. Lou, *Angew. Chem. Int. Ed.* **2018**, *57*, 15076.

[5] P. Zhang, X. F. Lu, J. Nai, S. Z. Zang, X. W. Lou, *Adv. Sci.* **2019**, *6*, 1900576.

[6] X. F. Lu, Y. Chen, S. Wang, S. Gao, X. W. Lou, *Adv. Mater.* **2019**, *31*, 1902339.

[7] M. Zhang, Q. Dai, H. Zheng, M. Chen, L. Dai, *Adv. Mater.* **2018**, *30*, 1705431.

[8] S. Dresp, F. Luo, R. Schmack, S. Kühl, M. Gliech, P. Strasser, *Energy Environ. Sci.* **2016**, *9*, 2020.

[9] X. F. Lu, L. Yu, J. Zhang, X. W. Lou, *Adv. Mater.* **2019**, *31*, 1900699.

[10] X. Li, B. Y. Guan, S. Gao, X. W. Lou, *Energy Environ. Sci.* **2019**, *12*, 648.

[11] X. F. Lu, L. Yu, X. W. Lou, *Sci. Adv.* **2019**, *5*, eaav6009.

[12] X. F. Lu, B. Y. Xia, S. Q. Zang, X. W. Lou, *Angew. Chem. Int. Ed.* **2020**, *59*, DOI: 10.1002/anie.201910309.

[13] H. Zhang, W. Zhou, T. Chen, B. Y. Guan, Z. Li, X. W. Lou, *Energy Environ. Sci.* **2018**, *11*, 1980.

[14] H. B. Wu, B. Y. Xia, L. Yu, X. Y. Yu, X. W. Lou, *Nat. Commun.* **2015**, *6*, 6512.

[15] B. Y. Guan, Y. Lu, Y. Wang, M. Wu, X. W. Lou, *Adv. Funct. Mater.* **2018**, *28*, 1706738.

[16] O. Kasian, J. P. Grote, S. Geiger, S. Cherevko, K. J. J. Mayrhofer, *Angew. Chem. Int. Ed.* **2018**, *57*, 2488.

[17] H. Zhang, Y. Liu, T. Chen, J. Zhang, J. Zhang, X. W. Lou, *Adv. Mater.* **2019**, *31*, 1904548.

[18] M. Huynh, C. Shi, S. J. L. Billinge, D. G. Nocera, *J. Am. Chem. Soc.* **2015**, *137*, 14887.

[19] M. W. Kanan, D. G. Nocera, *Science* **2008**, *321*, 1072.

[20] P. Chen, K. Xu, T. Zhou, Y. Tong, J. Wu, H. Cheng, X. Lu, H. Ding, C. Wu, Y. Xie, *Angew. Chem. Int. Ed.* **2016**, *55*, 2488.

[21] L. Xie, R. Zhang, L. Cui, D. Liu, S. Hao, Y. Ma, G. Du, A. M. Asiri, X. Sun, *Angew. Chem. Int. Ed.* **2017**, *56*, 1064.

[22] X. F. Lu, L. F. Gu, J. W. Wang, J. X. Wu, P. Q. Liao, G. R. Li, *Adv. Mater.* **2017**, *29*, 1604437.

[23] Y. Xu, W. Tu, B. Zhang, S. Yin, Y. Huang, M. Kraft, R. Xu, *Adv. Mater.* **2017**, *29*, 1605957.

[24] J. Wang, L. Gan, W. Zhang, Y. Peng, H. Yu, Q. Yan, X. Xia, X. Wang, *Sci. Adv.* **2018**, *4*, eaap7970.

[25] Y. P. Zhu, T. Y. Ma, M. Jaroniec, S. Z. Qiao, *Angew. Chem. Int. Ed.* **2017**, *56*, 1324.

[26] C. Liao, B. Yang, N. Zhang, M. Liu, G. Chen, X. Jiang, G. Chen, J. Yang, X. Liu, T. S. Chan, Y. J. Lu, R. Ma, W. Zhou, *Adv. Funct. Mater.* **2019**, *29*, 1904020.

[27] T. N. Huan, G. Rousse, S. Zanna, I. T. Lucas, X. Xu, N. Menguy, V. Mougel, M. Fontecave, *Angew. Chem. Int. Ed.* **2017**, *56*, 4792.

[28] Z. M. Chan, D. A. Kitchaev, J. N. Weker, C. Schnedermann, K. Lim, G. Ceder, W. Tumas, M. F. Toney, D. G. Nocera, *Proc. Natl. Acad. Sci. USA* **2018**, *115*, 5261.

[29] Y. Duan, S. Sun, Y. Sun, S. Xi, X. Chi, Q. Zhang, X. Ren, J. Wang, S. J. H. Ong, Y. Du, L. Gu, A. Grimaud, Z. J. Xu, *Adv. Mater.* **2019**, *31*, 1807898.

[30] X. Li, H. Wang, Z. Cui, Y. Li, S. Xin, J. Zhou, Y. Long, C. Jin, J. B. Goodenough, *Sci. Adv.* **2019**, *5*, eaav6262.

[31] L. Han, X. Y. Yu, X. W. Lou, *Adv. Mater.* **2016**, *28*, 4601.

[32] J. Liu, Y. Zheng, Z. Wang, Z. Lu, A. Vasileff, S. Z. Qiao, *Chem. Commun.* **2018**, *54*, 463.

[33] H. Wang, E. M. Feng, Y. M. Liu, C. Y. Zhang, *J. Mater. Chem. A* **2019**, *7*, 7777.

[34] L. J. Enman, M. B. Stevens, M. H. Dahan, M. R. Nellist, M. C. Toroker, S. W. Boettcher, *Angew. Chem. Int. Ed.* **2018**, *57*, 12840.

[35] B. Zhang, X. Zheng, O. Voznyy, R. Comin, M. Bajdich, M. García-Melchor, L. Han, J. Xu, M. Liu, L. Zheng, F. P. García de Arquer, C. T. Dinh, F. Fan, M. Yuan, E. Yassitepe, N. Chen, T. Regier, P. Liu, Y. Li, P. D. Luna, A. Janmohamed, H. L. Xin, H. Yang, A. Vojvodic, E. H. Sargent, *Science* **2016**, *352*, 333.

[36] L. Yu, J. F. Yang, B. Y. Guan, Y. Lu, X. W. Lou, *Angew. Chem. Int. Ed.* **2018**, *57*, 172.

[37] S. Yin, W. Tu, Y. Sheng, Y. Du, M. Kraft, A. Borgna, R. Xu, *Adv. Mater.* **2018**, *30*, 1705106.

[38] P. Cai, J. Huang, J. Chen, Z. Wen, *Angew. Chem. Int. Ed.* **2017**, *56*, 4858.

[39] K. Jayaramulu, J. Masa, O. Tomanec, D. Peeters, V. Ranc, A. Schneemann, R. Zboril, W. Schuhmann, R. A. Fischer, *Adv. Funct. Mater.* **2017**, *27*, 1700451.

[40] J. Nai, Y. Lu, L. Yu, X. Wang, X. W. Lou, *Adv. Mater.* **2017**, *29*, 1703870.

[41] K. Wan, J. Luo, C. Zhou, T. Zhang, J. Arbiol, X. Lu, B. W. Mao, X. Zhang, J. Fransaer, *Adv. Funct. Mater.* **2019**, *29*, 1900315.

[42] X. Y. Yu, X. W. Lou, *Adv. Energy Mater.* **2018**, *8*, 1701592.

[43] E. Hu, Y. Feng, J. Nai, D. Zhao, Y. Hu, X. W. Lou, *Energy Environ. Sci.* **2018**, *11*, 872.

[44] P. He, X. Y. Yu, X. W. Lou, *Angew. Chem. Int. Ed.* **2017**, *56*, 3897.

[45] X. Ren, R. Ge, Y. Zhang, D. Liu, D. Wu, X. Sun, B. Du, Q. Wei, *J. Mater. Chem. A* **2017**, *5*, 7291.

[46] C. Xie, Y. Wang, D. Yan, L. Tao, S. Wang, *Nanoscale* **2017**, *9*, 16059.

[47] J. M. V. Nsanzimana, L. Gong, R. Dangol, V. Reddu, V. Jose, B. Y. Xia, Q. Yan, J. M. Lee, X. Wang, *Adv. Energy Mater.* **2019**, *9*, 1901503.

[48] C. Walter, P. W. Menezes, S. Orthmann, J. Schuch, P. Connor, B. Kaiser, M. Lerch, M. Driess, *Angew. Chem. Int. Ed.* **2018**, *57*, 698.

[49] S. Zhao, M. Li, M. Han, D. Xu, J. Yang, Y. Lin, N. E. Shi, Y. Lu, R. Yang, B. Liu, Z. Dai, J. Bao, *Adv. Funct. Mater.* **2018**, *28*, 1706018.

[50] M. A. R. Anjum, M. H. Lee, J. S. Lee, *ACS Catal.* **2018**, *8*, 8296.

[51] H. Jiang, Q. He, X. Li, X. Su, Y. Zhang, S. Chen, S. Zhang, G. Zhang, J. Jiang, Y. Luo, P. M. Ajayan, L. Song, *Adv. Mater.* **2019**, *31*, 1805127.

[52] K. Fominykh, J. M. Feckl, J. Sicklinger, M. Döblinger, S. Böcklein, J. Ziegler, L. Peter, J. Rathousky, E. W. Scheidt, T. Bein, D. Fattakhova-Rohlfing, *Adv. Funct. Mater.* **2014**, *24*, 3123.

[53] I. C. Man, H. Y. Su, F. Calle-Vallejo, H. A. Hansen, J. I. Martínez, N. G. Inoglu, J. Kitchin, T. F. Jaramillo, J. K. Nørskov, J. Rossmeisl, *ChemCatChem* **2011**, *3*, 1159.

[54] T. R. Cook, D. K. Dogutan, S. Y. Reece, Y. Surendranath, T. S. Teets, D. G. Nocera, *Chem. Rev.* **2010**, *110*, 6474.

[55] S. Anantharaj, S. R. Ede, K. Karthick, S. S. Sankar, K. Sangeetha, P. E. Karthik, S. Kundu, *Energy Environ. Sci.* **2018**, *11*, 744.

[56] H. Vrubel, T. Moehl, M. Grätzel, X. Hu, *Chem. Commun.* **2013**, *49*, 8985.

[57] J. D. Benck, T. R. Hellstern, J. Kibsgaard, P. Chakthranont, T. F. Jaramillo, *ACS Catal.* **2014**, *4*, 3957.

[58] S. Anantharaj, P. E. Karthik, S. Kundu, *Catal. Sci. Technol.* **2017**, *7*, 882.

[59] S. Anantharaj, S. R. Ede, K. Sakthikumar, K. Karthick, S. Mishra, S. Kundu, *ACS Catal.* **2016**,

6, 8069.

[60] D. Voiry, M. Chhowalla, Y. Gogotsi, N. A. Kotov, Y. Li, R. M. Penner, R. E. Schaak, P. S. Weiss, *ACS Nano* **2018**, *12*, 9635.

[61] C. Tang, R. Zhang, W. Lu, Z. Wang, D. Liu, S. Hao, G. Du, A. M. Asiri, X. Sun, *Angew. Chem. Int. Ed.* **2017**, *56*, 842.

[62] F. Yu, H. Zhou, Y. Huang, J. Sun, F. Qin, J. Bao, W. A. Goddard III, S. Chen, Z. Ren, *Nat. Commun.* **2018**, *9*, 2551.

[63] C. Wang, H. Yang, Y. Zhang, Q. Wang, *Angew. Chem. Int. Ed.* **2019**, *58*, 6099.

[64] Z. P. Wu, S. Shan, Z. H. Xie, N. Kang, K. Park, E. Hopkins, S. Yan, A. Sharma, J. Luo, J. Wang, V. Petkov, L. Wang, C. J. Zhong, *ACS Catal.* **2018**, *8*, 11302.

[65] M. Liu, L. Wang, K. Zhao, S. Shi, Q. Shao, L. Zhang, X. Sun, Y. Zhao, J. Zhang, *Energy Environ. Sci.* **2019**, *12*, 2890.

[66] B. Bayatsarmadi, Y. Zheng, A. Vasileff, S. Z. Qiao, *Small* **2017**, *13*, 1700191.

[67] Y. Tong, P. Chen, T. Zhou, K. Xu, W. Chu, C. Wu, Y. Xie, *Angew. Chem. Int. Ed.* **2017**, *56*, 7121.

[68] Q. Zhao, Z. Yan, C. Chen, J. Chen, *Chem. Rev.* **2017**, *117*, 10121.

[69] S. Peng, F. Gong, L. Li, D. Yu, D. Ji, T. Zhang, Z. Hu, Z. Zhang, S. Chou, Y. Du, S. Ramakrishna, *J. Am. Chem. Soc.* **2018**, *140*, 13644.

[70] J. Sun, N. Guo, Z. Shao, K. Huang, Y. Li, F. He, Q. Wang, *Adv. Energy Mater.* **2018**, *8*, 1800980.

[71] Y. Liu, Y. Ying, L. Fei, Y. Liu, Q. Hu, G. Zhang, S. Y. Pang, W. Lu, C. L. Mak, X. Luo, L. Zhou, M. Wei, H. Huang, *J. Am. Chem. Soc.* **2019**, *141*, 8136.

[72] X. Wang, L. Yu, B. Y. Guan, S. Song, X. W. Lou, *Adv. Mater.* **2018**, *30*, 1801211.

[73] G. Chen, W. Zhou, D. Guan, J. Sunarso, Y. Zhu, X. Hu, W. Zhang, Z. Shao, *Sci. Adv.* **2017**, *3*, e1603206.

[74] N. I. Kim, Y. J. Sa, T. S. Yoo, S. R. Choi, R. A. Afzal, T. Choi, Y. S. Seo, K. S. Lee, J. Y. Hwang, W. S. Choi, S. H. Joo, J. Y. Park, *Sci. Adv.* **2018**, *4*, eaap9360.

[75] H. Wang, J. Wang, Y. Pi, Q. Shao, Y. Tan, X. Huang, *Angew. Chem. Int. Ed.* **2019**, *58*, 2316.

[76] D. McAteer, I. J. Godwin, Z. Ling, A. Harvey, L. He, C. S. Boland, V. Vega-Mayoral, B. Szydłowska, A. A. Rovetta, C. Backes, J. B. Boland, X. Chen, M. E. G. Lyons, J. N. Coleman, *Adv.*

Energy Mater. **2018**, *8*, 1702965.

[77] Q. Zhou, Y. Chen, G. Zhao, Y. Lin, Z. Yu, X. Xu, X. Wang, H. K. Liu, W. Sun, S. X. Dou, *ACS Catal.* **2018**, *8*, 5382.

[78] R. Liu, Y. Wang, D. Liu, Y. Zou, S. Wang, *Adv. Mater.* **2017**, *29*, 1701546.

[79] M. S. Burke, L. J. Enman, A. S. Batchellor, S. Zou, S. W. Boettcher, *Chem. Mater.* **2015**, *27*, 7549.

[80] M. B. Stevens, C. D. M. Trang, L. J. Enman, J. Deng, S. W. Boettcher, *J. Am. Chem. Soc.* **2017**, *139*, 11361.

[81] C. Xuan, W. Lei, J. Wang, T. Zhao, C. Lai, Y. Zhu, Y. Sun, D. Wang, *J. Mater. Chem. A* **2019**, *7*, 12350.

[82] X. Y. Yu, Y. Feng, B. Y. Guan, X. W. Lou, U. Paik, *Energy Environ. Sci.* **2016**, *9*, 1246.

[83] H. Zhang, W. Zhou, J. Dong, X. F. Lu, X. W. Lou, *Energy Environ. Sci.* **2019**, *12*, 3348.

[84] B. Y. Guan, L. Yu, X. W. Lou, *Angew. Chem. Int. Ed.* **2017**, *56*, 2386.

[85] G. Hu, J. Xiang, J. Li, P. Liu, R. N. Ali, B. Xiang, *J. Catal.* **2019**, *371*, 126.

[86] S. Xue, L. Chen, Z. Liu, H. M. Cheng, W. Ren, *ACS Nano* **2018**, *12*, 5297.

[87] M. Cabán-Acevedo, M. L. Stone, J. R. Schmidt, J. G. Thomas, Q. Ding, H. C. Chang, M. L. Tsai, J. H. He, S. Jin, *Nat. Mater.* **2015**, *14*, 1245.

[88] B. Song, K. Li, Y. Yin, T. Wu, L. Dang, M. Cabán-Acevedo, J. Han, T. Gao, X. Wang, Z. Zhang, J. R. Schmidt, P. Xu, S. Jin, *ACS Catal.* **2017**, *7*, 8549.

[89] Y. Gershinsky, D. Zitoun, *ACS Catal.* **2018**, *8*, 8715.

[90] J. M. V. Nsanzimana, Y. Peng, Y. Y. Xu, L. Thia, C. Wang, B. Y. Xia, X. Wang, *Adv. Energy Mater.* **2018**, *8*, 1701475.

[91] F. Guo, Y. Wu, H. Chen, Y. Liu, L. Yang, X. Ai, X. Zou, *Energy Environ. Sci.* **2019**, *12*, 684.

[92] J. Huang, Y. Sun, X. Du, Y. Zhang, C. Wu, C. Yan, Y. Yan, G. Zou, W. Wu, R. Lu, Y. Li, J. Xiong, *Adv. Mater.* **2018**, *30*, 1803367.

[93] Y. Guo, T. Wang, J. Chen, J. Zheng, X. Li, K. K. Ostrikov, *Adv. Energy Mater.* **2018**, *8*, 1800085.

[94] X. F. Lu, P. Q. Liao, J. W. Wang, J. X. Wu, X. W. Chen, C. T. He, J. P. Zhang, G. R. Li, X. M. Chen, *J. Am. Chem. Soc.* **2016**, *138*, 8336.

[95] M. Blasco-Ahicart, J. Soriano-López, J. J. Carbó, J. M. Poblet, J. R. Galan-Mascaros, *Nat.*

Chem. **2018**, *10*, 24.

[96] M. Huynh, D. K. Bediako, D. G. Nocera, *J. Am. Chem. Soc.* **2014**, *136*, 6002.

[97] R. Frydendal, E. A. Paoli, I. Chorkendorff, J. Rossmeisl, I. E. L. Stephens, *Adv. Energy Mater.* **2015**, *5*, 1500991.

[98] L. Zhao, Q. Cao, A. Wang, J. Duan, W. Zhou, Y. Sang, H. Liu, *Nano Energy* **2018**, *45*, 118.

[99] J. O. Bockris, *J. Chem. Phys.* **1956**, *24*, 817.

[100] H. Dau, C. Limberg, T. Reier, M. Risch, S. Roggan, P. Strasser, *ChemCatChem* **2010**, *2*, 724.

[101] X. Shi, S. Siahrostami, G. L. Li, Y. Zhang, P. Chakthranont, F. Studt, T. F. Jaramillo, X. Zheng, J. K. Nørskov, *Nat. Commun.* **2017**, *8*, 701.

[102] J. K. Nørskov, J. Rossmeisl, A. Logadottir, L. Lindqvist, J. R. Kitchin, T. Bligaard, H. Jónsson, *J. Phys. Chem. B* **2004**, *108*, 17886.

[103] J. O. Bockris, T. Otagawa, *J. Electrochem. Soc.* **1984**, *131*, 290.

[104] R. Subbaraman, D. Tripkovic, K. C. Chang, D. Strmcnik, A. P. Paulikas, P. Hirunsit, M. Chan, J. Greeley, V. Stamenkovic, N. M. Markovic, *Nat. Mater.* **2012**, *11*, 550.

[105] J. Kibsgaard, I. Chorkendorff, *Nat. Energy* **2019**, *4*, 430.

[106] A. Vojvodic, J. K. Nørskov, *Science* **2011**, *334*, 1355.

[107] J. K. Nørskov, T. Bligaard, J. Rossmeisl, C. H. Christensen, *Nat. Chem.* **2009**, *1*, 37.

[108] J. Suntivich, K. J. May, H. A. Gasteiger, J. B. Goodenough, Y. Shao-Horn, *Science* **2011**, *334*, 1383.

[109] S. Trasatti, *J. Electroanal. Chem.* **1980**, *111*, 125.

[110] M. D. Porosoff, B. Yan, J. G. Chen, *Energy Environ. Sci.* **2016**, *9*, 62.

[111] B. M. Tackett, W. Sheng, J. G. Chen, *Joule* **2017**, *1*, 253.

[112] M. Schalenbach, G. Tjarks, M. Carmo, W. Lueke, M. Mueller, D. Stolten, *J. Electrochem. Soc.* **2016**, *163*, F3197.

[113] Y. Xin, X. Kan, L. Y. Gan, Z. Zhang, *ACS Nano* **2017**, *11*, 10303.

[114] Z. Wang, Q. Li, H. Xu, C. Dahl-Petersen, Q. Yang, D. Cheng, D. Cao, F. Besenbacher, J. V. Lauritsen, S. Helveg, M. Dong, *Nano Energy* **2018**, *49*, 634.

[115] Z. Wang, H. H. Wu, Q. Li, F. Besenbacher, Y. Li, X. C. Zeng, M. Dong, *Adv. Sci.* **2019**, DOI: 10.1002/advs.201901382.

[116] Y. Wang, C. Xie, Z. Zhang, D. Liu, R. Chen, S. Wang, *Adv. Funct. Mater.* **2018**, *28*, 1703363.

[117] J. Shan, C. Guo, Y. Zhu, S. Chen, L. Song, M. Jaroniec, Y. Zheng, S. Z. Qiao, *Chem* **2019**, *5*, 445.

[118] J. Shan, T. Ling, K. Davey, Y. Zheng, S. Z. Qiao, *Adv. Mater.* **2019**, *31*, 1900510.

[119] J. Shan, Y. Zheng, B. Shi, K. Davey, S. Z. Qiao, *ACS Energy Lett.* **2019**, *4*, 2719.

[120] M. Chen, L. Wang, H. Yang, S. Zhao, H. Xu, G. Wu, *J. Power Sources* **2018**, *375*, 277.

[121] X. Zou, Y. Zhang, *Chem. Soc. Rev.* **2015**, *44*, 5148.

[122] C. C. L. McCrory, S. Jung, I. M. Ferrer, S. M. Chatman, J. C. Peters, T. F. Jaramillo, *J. Am. Chem. Soc.* **2015**, *137*, 4347.

[123] M. G. Mavros, T. Tsuchimochi, T. Kowalczyk, A. McIsaac, L. P. Wang, T. V. Voorhis, *Inorg. Chem.* **2014**, *53*, 6386.

[124] K. Zhu, X. Zhu, W. Yang, *Angew. Chem. Int. Ed.* **2019**, *58*, 1252.

[125] F. Chang, S. Shan, V. Petkov, Z. Skeete, A. Lu, J. Ravid, J. Wu, J. Luo, G. Yu, Y. Ren, C. J. Zhong, *J. Am. Chem. Soc.* **2016**, *138*, 12166.

[126] M. Huynh, T. Ozel, C. Liu, E. C. Lau, D. G. Nocera, *Chem. Sci.* **2017**, *8*, 4779.

Figures and Captions

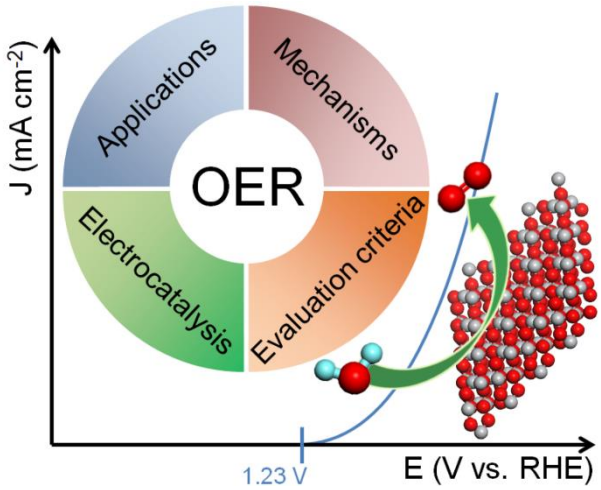

Figure 1. Schematic illustration of the OER on a model catalyst surface, and its main research contents discussed in this review.

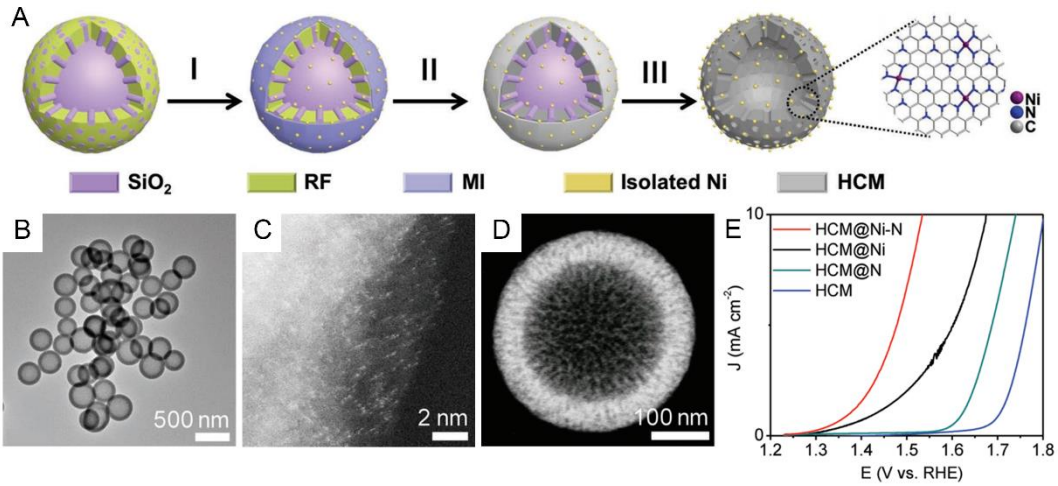

Figure 2. (A) A schematic illustration of the fabrication process of HCM@Ni-N: (I) coating of methylimidazole-Ni (MI-Ni), (II) annealing process, and (III) etching treatment. RF denotes resorcinol formaldehyde and MI represents methylimidazole. (B) A representative TEM image of the HCM@Ni-N nanospheres. (C) The atomic resolution ADF-STEM image, and (D) HAADF-STEM image of HCM@Ni-N. (E) OER polarization curves of different catalysts in 1.0 M KOH electrolyte. Reproduced with permission.[17] Copyright 2019, WILEY-VCH.

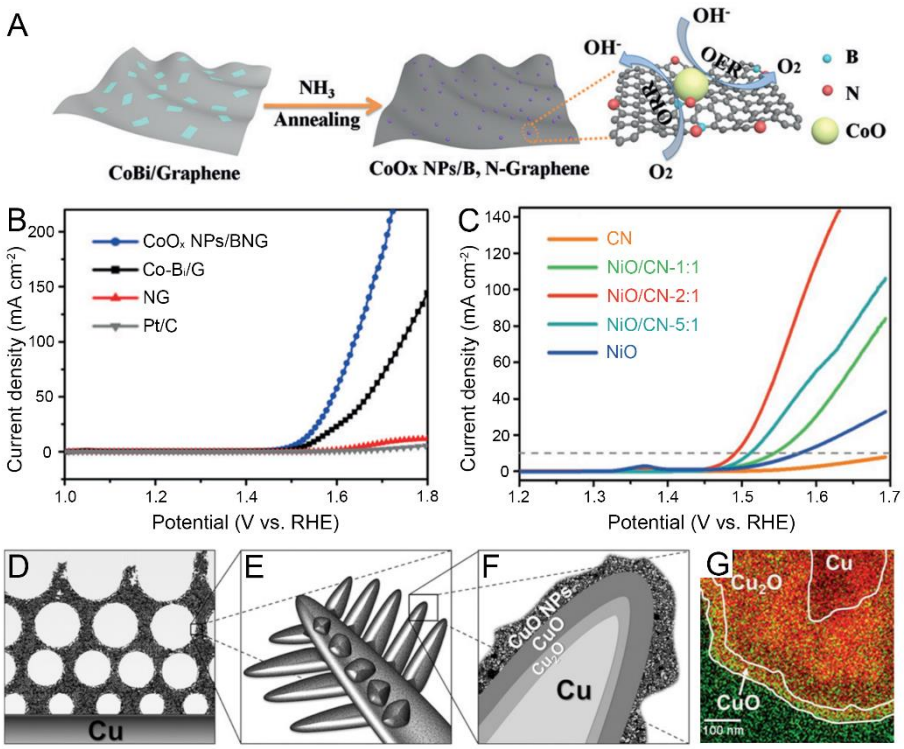

Figure 3. (A) An illustration of the preparation of CoO_x NPs grown on B,N-decorated graphene sheets. (B) OER performance of catalysts in 0.1 M KOH electrolyte. Reproduced with permission.[67] Copyright 2017, WILEY-VCH. (C) OER polarization curves of different catalysts in 1.0 M KOH electrolyte. Reproduced with permission.[26] Copyright 2019, WILEY-VCH. (D-F) Synthetic strategy for the Cu/CuO hybrid nanomaterial: (D) macropore foam generated by hydrogen bubble assistance, (E) an illustration of the dendritic structured Cu/CuO nanomaterial, (F) a schematic diagram of the magnified view of the zoomed region in (E). (G) STEM-XEDS patterns of the materials (O in green and Cu in red). Reproduced with permission.[27] Copyright 2017, WILEY-VCH.

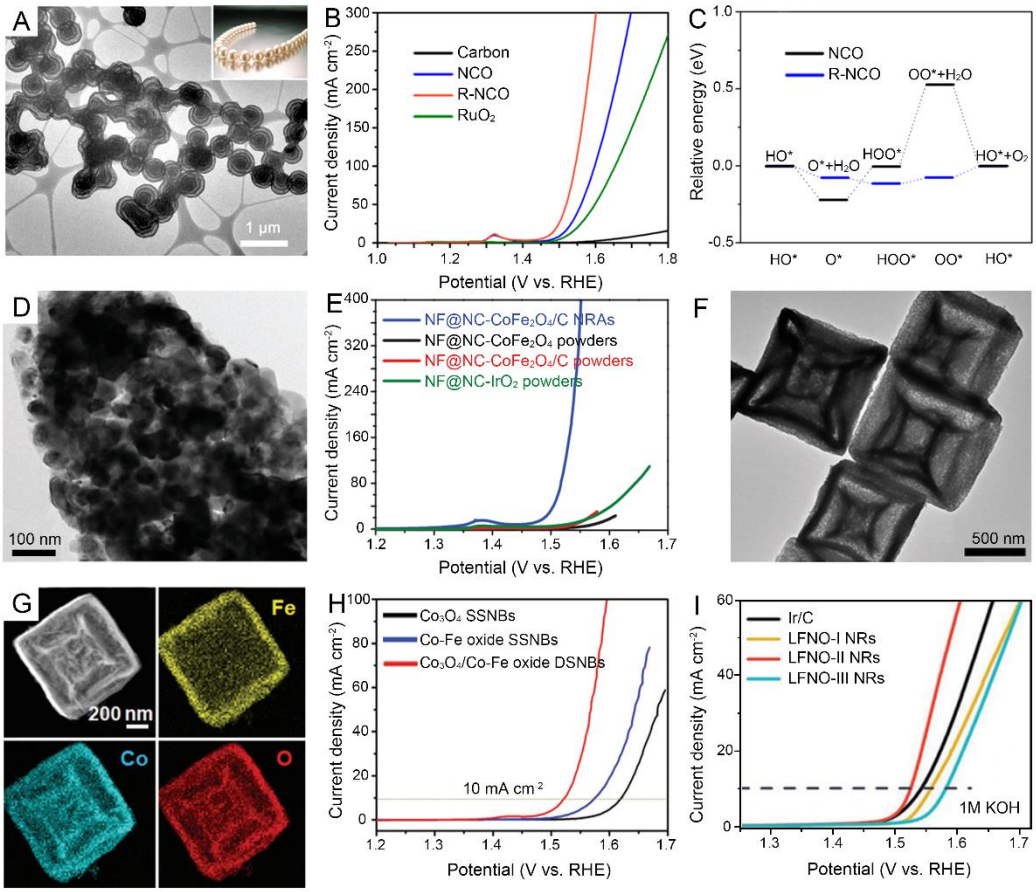

Figure 4. (A) A representative TEM image of R-NCO. The inset in (A) shows a photograph of a necklace. (B) OER polarization curves of electrocatalysts in 1.0 M KOH electrolyte. (C) Energy diagrams of the OER on NCO and R-NCO at the equilibrium potential of 1.23 V. Reproduced with permission.[69] Copyright 2018, American Chemical Society. (D) A representative TEM image of a $CoFe_2O_4$/C nanorod. (E) OER performance of different catalysts in 1.0 M KOH electrolyte. Reproduced with permission.[22] Copyright 2017, WILEY-VCH. (F) A representative TEM image of the Co_3O_4/Co-Fe oxide DSNBs. (G) HAADF-STEM images of an individual Co_3O_4/Co-Fe oxide DSNB. (H) LSV curves of different catalysts recorded in 1.0 M KOH electrolyte. Reproduced with permission.[72] Copyright 2018, WILEY-VCH. (I) OER polarization curves of double perovskite LFNO catalysts in 1.0 M KOH electrolyte. Reproduced with permission.[75] Copyright 2019, WILEY-VCH.

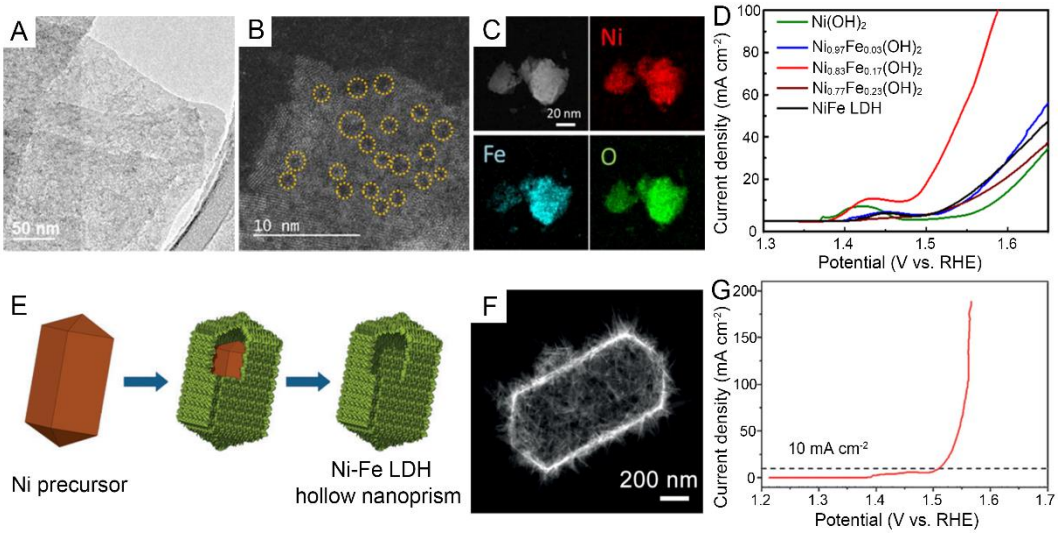

Figure 5. (A) A representative TEM image, and (B) HAADF-STEM image of $Ni_{0.83}Fe_{0.17}(OH)_2$ nanosheet. (C) HAADF-STEM image and the corresponding elemental maps of $Ni_{0.83}Fe_{0.17}(OH)_2$. (D) OER performance of different electrocatalysts recorded in 1.0 M KOH electrolyte. Reproduced with permission.[77] Copyright 2018, American Chemical Society. (E) Schematic illustration of the formation of hierarchical Ni-Fe LDH hollow nanoprisms. (F) HAADF-STEM image of a single Ni-Fe LDH hollow nanoprism. (G) OER polarization curve of the Ni-Fe LDH hollow nanoprism electrocatalyst. Reproduced with permission.[36] Copyright 2018, WILEY-VCH.

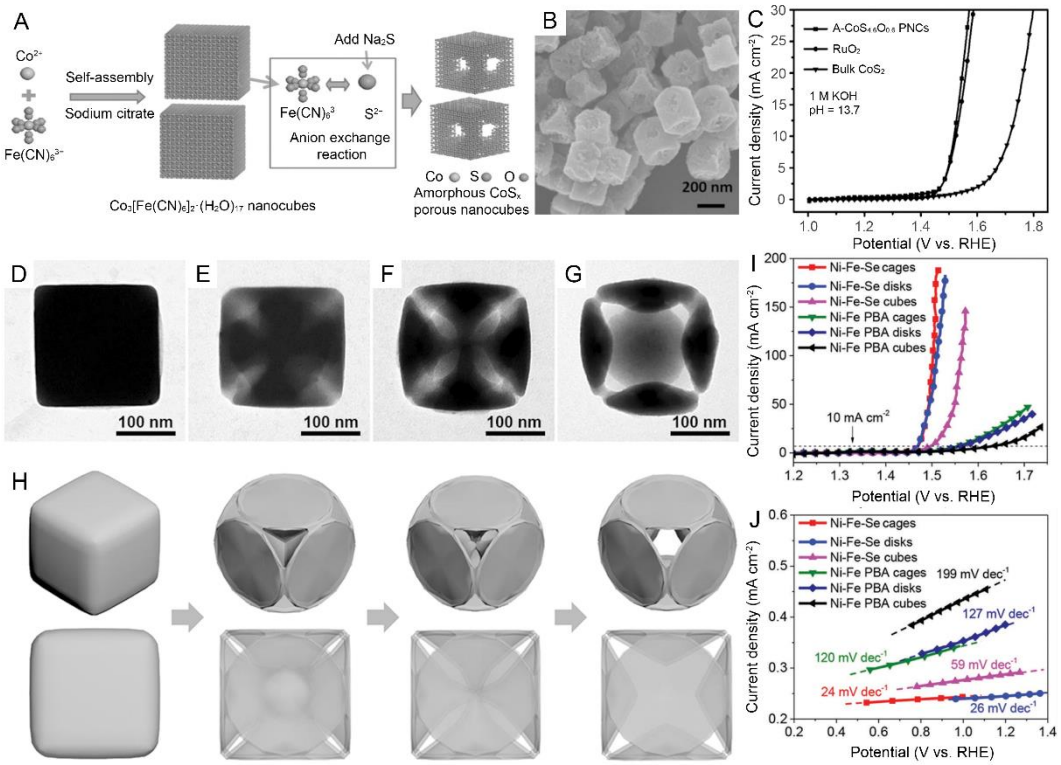

Figure 6. (A) A schematic illustration of the fabrication process for A-$CoS_{4.6}O_{0.6}$ PNCs. (B) A representative FESEM image of A-$CoS_{4.6}O_{0.6}$ PNCs. (C) OER polarization curves of different catalysts measured in 1.0 M KOH solution. Reproduced with permission.[38] Copyright 2017, WILEY-VCH. (D-G) TEM images of the products observed along the ammonia etching time at (D) 0 min, (E) 1 min, (F) 3 min, (G) 5 min for the preparation of the Ni-Fe PBA nanocages. (H) A corresponding schematic diagram showing the structural evolution process from Ni-Fe PBA nanocubes to nanocages. (I) OER polarization curves, and (J) the corresponding Tafel slope of six different catalysts in 1.0 M KOH electrolyte. Reproduced with permission.[40] Copyright 2017, WILEY-VCH.

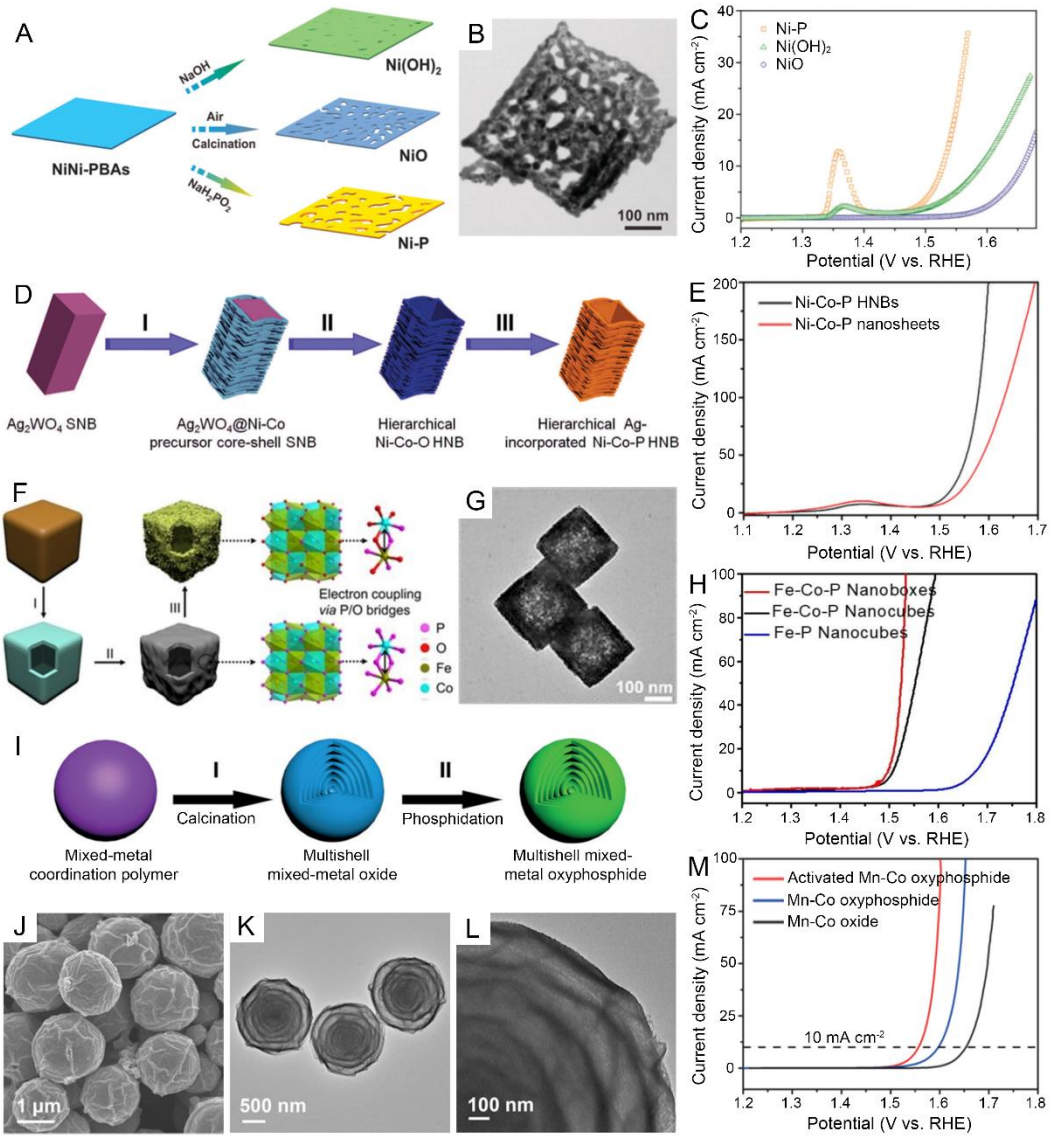

Figure 7. (A) Schematic diagram of the fabrication process of NiNi-PBA-derived $Ni(OH)_2$, NiO, and Ni-P nanoplates. (B) TEM image of an individual Ni-P nanoplate. (C) LSV curves of different Ni-based nanoplates in 1.0 M KOH electrolyte. Reproduced with permission.[82] Copyright 2016, The Royal Society of Chemistry. (D) A schematic diagram of the fabrication process of Ni-Co-P HNBs: (I) precursor synthesis, (II) annealing and etching treatments, and (III) phosphorization process. (E) OER polarization curves of Ni-Co-P HNBs and nanosheets in 1.0 M KOH electrolyte. Reproduced with permission.[43] Copyright 2018, The Royal Society of Chemistry. (F) Schematic illustration of the preparation process of Fe-Co-P nanobox pre-catalysts: (I) synthesis of the Fe-Co PBA nanoboxes, (II) phosphorization process, and (III) catalytically structural evolution. (G) TEM image of the Fe-Co-P nanoboxes. (H) OER performance of different electrocatalysts in 1.0 M KOH electrolyte. Reproduced with permission.[83] Copyright 2019, The Royal Society of Chemistry. (I) An illustration of the preparation process for the multishell mixed-metal oxyphosphide particle. (J) FESEM, and (K-L) TEM images of the multishell MnCo oxyphosphide particles. (M) OER performance of different catalysts in 1.0 M KOH electrolyte. Reproduced with permission.[84] Copyright 2017, WILEY-VCH.

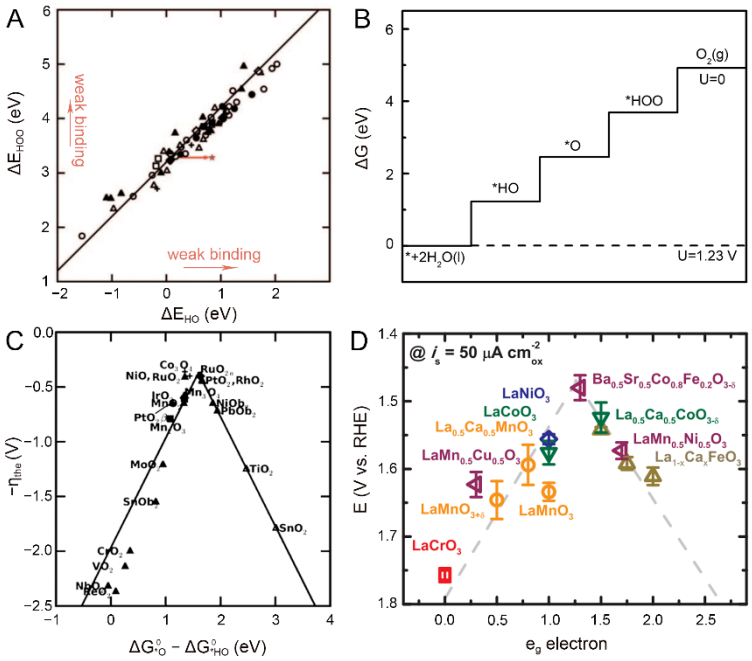

Figure 8. (A) The relationship between the adsorption energies of *OOH and *OH on a series of oxide OER catalysts. (B) Free energy diagram at U = 0 and U = 1.23 V for the OER on the ideal catalyst. (C) The volcano plot illustrating the relationship between the OER activities against the standard free energy of $\Delta G^{o}_{*O} - \Delta G^{o}_{*OH}$, on a set of OER catalysts. Reproduced with permission.[53] Copyright 2011, WILEY-VCH. (D) The volcano plot showing the relation between the OER overpotential (at 50 μA cm^{-2}) and the occupancy of the e_g electron of the transition metal. Reproduced with permission.[108] Copyright 2011, American Association for the Advancement of Science.

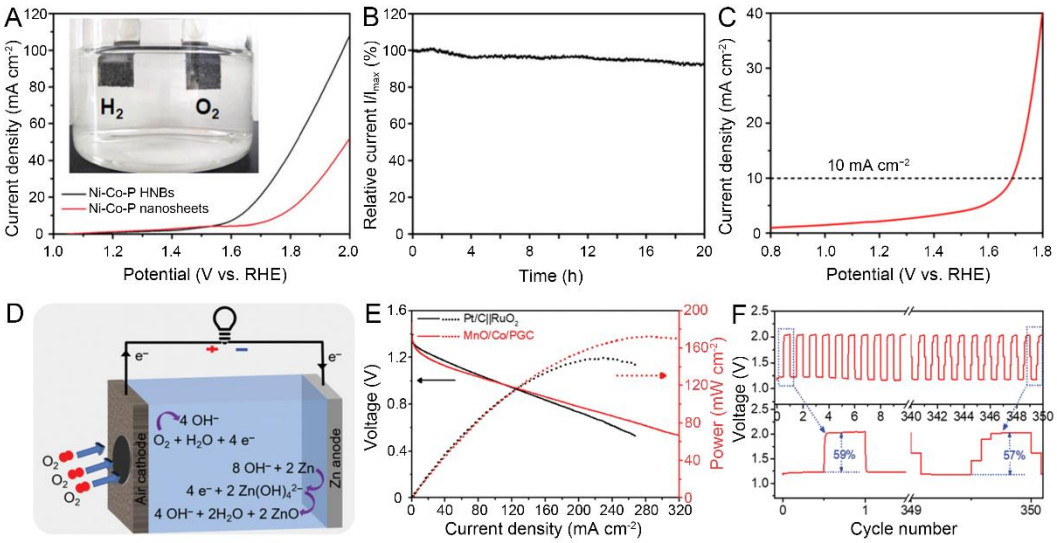

Figure 9. (A) Overall water splitting polarization curves of Ni-Co-P HNBs and nanosheets. The inset image in (A) displays a photograph of the overall water splitting cell. (B) The I-t curve of the Ni-Co-P HNBs for the overall water splitting at 1.62 V (vs. RHE). Reproduced with permission.[43] Copyright 2018, The Royal Society of Chemistry. (C) LSV curve of CoFe oxyphosphide microtubes for the overall water splitting. Reproduced with permission.[5] Copyright 2019, WILEY-VCH. (D) A schematic illustration of the ZAB. (E) Discharge polarization curves and power density plots of two custom-designed Zn-air batteries powered by Pt/C||RuO_2 and MnO/Co/PGC. (F) Durability test with MnO/Co/PGC as the cathode catalyst at a current density of 10 mA cm^{-2}. Reproduced with permission.[6] Copyright 2019, WILEY-VCH.

Table 1. Summary of various non-noble-metal-based OER electrocatalysts and their OER performance.

Catalysts	Electrolytes	Substrates	Catalyst loading (mg cm^{-2})	Overpotential @10 mA cm^{-2} (mV)	Tafel slope (mV dec^{-1})	Ref.
Ni NPs/ N-doped graphene	1.0 M KOH	GCE[a]	0.31	280	45	[23]
Ni atom/N-doped carbon	1.0 M KOH	CFP[b]	1.6	304	76	[17]
CoO_x NPs/BNG	0.1 M KOH	GCE	N/A[c]	295	57	[67]
NiO/carbon nitride	1.0 M KOH	GCE	0.285	261	58.9	[26]
CuO/Cu foam	1 M NaOH	Cu foam	N/A	290	64	[27]
Reduced $NiCo_2O_4$ NPs	1.0 M KOH	Ni foam	2.5	240	50	[69]
$CoFe_2O_4$ nanorod array	1.0 M KOH	Ni foam	1.03	240	45	[22]
Co_3O_4/Co-Fe oxide DSNBs	1.0 M KOH	GCE	0.25	297	61	[72]
$LaFe_xNi_{1-x}O_3$ nanorod	1.0 M KOH	GCE	0.81	302	50	[75]
$Ni_{0.83}Fe_{0.17}(OH)_2$ nanosheets	1.0 M KOH	GCE	0.204	245	61	[77]
CoFe LDHs nanosheets	1.0 M KOH	Ni foam	0.408	232	36	[78]
Ni-Fe LDH nanosheets	1.0 M KOH	GCE	0.16	280	49.4	[36]
FeCoW oxyhydroxide	1.0 M KOH	GCE	0.21	223	37	[35]
A-$CoS_{4.6}O_{0.6}$ PNCs	1.0 M KOH	GCE	0.8	290	67	[38]
Ni-Fe diselenide nanocages	1.0 M KOH	GCE	0.1	240	24	[40]
NiP nanoplates	1.0 M KOH	GCE	0.20	300	64	[82]
Ni-Co-P nanoboxes	1.0 M KOH	GCE	0.25	330	96	[44]
Fe-Co-P nanoboxes	1.0 M KOH	CFP	0.3	269	31	[83]
Co-Pi nanoarrays	0.1 M PBS[d]	Ti mesh	0.97	450	187	[21]
Fe-Co-2.3Ni-B	1.0 M KOH	GCE	0.3	274	38	[90]
Mn_3N_2	1.0 M KOH	Ni foam	3	270	101	[48]

[a] GCE stands for glassy carbon electrode; [b] CFP stands for carbon fiber paper; [c] N/A denotes not available; [d] PBS stands for phosphate-buffered saline.

For Table of Contents Entry

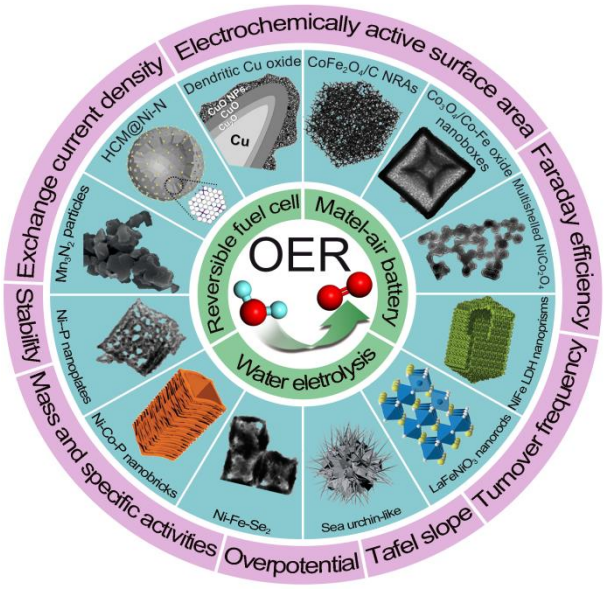

This review summarizes the evaluation criteria, recent advancements of non-noble-metal-based electrocatalysts, reaction mechanisms, and some practical applications of the oxygen evolution reaction (OER). Although a great stride has been made in the past decades, the current state of non-noble-metal-based OER electrocatalysts is still facing many challenges, which are discussed together with some useful perspectives and future directions.